POST-PERFORATION FLOW MODELS FOR THE API RECOMMENDED PRACTICES 19B

by

Alireza Roostapour

ProQuest Number: 10794873

All rights reserved

INFORMATION TO ALL USERS
The quality of this reproduction is dependent upon the quality of the copy submitted.

In the unlikely event that the author did not send a complete manuscript
and there are missing pages, these will be noted. Also, if material had to be removed,
a note will indicate the deletion.

ProQuest 10794873

Published by ProQuest LLC (2018). Copyright of the Dissertation is held by the Author.

All rights reserved.
This work is protected against unauthorized copying under Title 17, United States Code
Microform Edition © ProQuest LLC.

ProQuest LLC.
789 East Eisenhower Parkway
P.O. Box 1346
Ann Arbor, MI 48106 – 1346

A thesis submitted to the Faculty and Board of Trustees of the Colorado School of Mines in partial fulfillment of the requirements for the degree of *Master of Science* (Petroleum Engineering).

Golden Colorado

Date: 6/17/05

Signed: Alireza Roostapour
Alireza Roostapour

Approved: Turhan Yildiz
Dr. Turhan Yildiz
Thesis Advisor

Golden Colorado

Date: June 20, 2005

Craig W. Van Kirk
Dr. Craig W. Van Kirk
Professor and Head,
Department of Petroleum
Engineering

ABSTRACT

Relative merits of well perforators are rated based on a testing procedure and an evaluation method proposed by American Petroleum Institute (API). The API procedure and analysis method are published in API RP 19B "Recommended Practices for Evaluation of Well Perforators". In this procedure, a cylindrically shaped core target is perforated with a single shaped charge. During perforating, high pressures are generated and the core target is exposed to very high stresses. Due to high stress, jet perforators crush the rock around the perforation tunnel and decrease its permeability. API recommends running post-perforation flow tests to measure the degree and extent of the permeability damage caused by perforating charge. API RP 19B describes the post-perforation flow tests with complicated flow geometries in detail. The permeability damage in the perforated core target is quantified in terms of core flow efficiency (CFE).

In this thesis study, analytical models to analyze the post-perforation flow tests conducted on the laboratory apparatus with axial, semi-radial, and radial-axial configurations are developed. The analytical models are obtained by solving the two-dimensional diffusivity equation. The analytical models consider arbitrary damage distribution and variable radius along the perforation axis.

The analytical solutions are in the form of a Fourier series. The models are coded in a FORTRAN environment. The computer codes are included in this text. The proposed solutions are compared against the existing numerical models and verified. The analytical solutions are general, available to public, and very fast and inexpensive to compute.

Post-perforation flow tests described in API 19B may be analyzed using the analytical models. The primary use of the analytical model is to calculate the core flow efficiency.

After verifying their accuracy, the analytical models are used to evaluate the validity of the API recommended procedure and analysis technique. It is demonstrated that the post-perforation flow geometry, core/perforation dimensions, permeability anisotropy, and the degree of formation damage control CFE. The same degree of formation damage yields different CFE in different post-perforation flow geometries.

Axial CFE values are markedly influenced by the size of the core target. Hence, post-perforation flow tests should not be conducted on the axial configuration. Radial-axial CFE values do not seem to be affected by the core length; however, they are influenced by the core diameter. To have a stabilized radial-axial CFE value, core radius should be greater than 7 in.

CFE measured on the perforated core may not be a good indicator for the productivity of the perforated well in subsurface conditions. There exists a general trend that a higher CFE on the core may translate to a higher well productivity. However, when it comes to actual numerical values, CFE and productivity ratio of a perforated well are not meaningfully related.

It is recommended to convert the CFE value determined on a perforated core to an equivalent skin factor. Equivalent skin factor may be directly used in the productivity models developed for perforated wells. A method to convert the CFE data to an equivalent skin factor is presented. A procedure to rescale the skin factor from core targets to a perforated well is introduced.

TABLE OF CONTENTS

Page No.

ABSTRACT iii

LIST OF FIGURES vii

LIST OF TABLES ix

ACKNOWLEDGEMENT x

INTRODUCTION 1

CHAPTER 1 LITERATURE REVIEW 4

1.1..Introduction 4

1.2..API RP 19B 4

1.3..Flow Models for Post-Perforation Flow Tests 10

1.4..Inflow Models for Perforated Wells 13

CHAPTER 2 POST-PERFORATION FLOW MODELS 15

2.1..Introduction 15

2.2 Model for Axial Laboratory Flow Target 17

2.2.1 Case 1; $\beta = 0$ 21

2.2.2 Case 2; $\beta = -\lambda^2 < 0$ 22

2.2.3 Case 3; $b = \lambda^2 > 0$ 23

2.3 Model for Semi-Radial Laboratory Flow Target 35

2.3.1 Case 1; $\beta = 0$ 37

2.3.2 Case 2; $\beta = -\lambda^2 < 0$ 38

2.3.3 Case 3; $\beta = \lambda^2 > 0$ 39

2.4 Model for Radial-Axial Laboratory Flow Target 48

2.4.1 Case 1; $\beta = 0$ 49

2.4.2 Case 2; $\beta = -\lambda^2 < 0$ 50
2.4.3 Case 3; $\beta = \lambda^2 > 0$ 50
CHAPTER 3 VERIFICATION OF ANALYTICAL FLOW MODELS 54
3.1 Introduction 54
3.2 Verification of Axial Model 54
3.3 Verification of Radial-Axial Model 57
3.4..Verification of Semi-Radial Model 58
CHAPTER 4 APPLICATIONS AND DISCUSSION 60
4.1 Introduction 60
4.2 Effect of Test Configuration on Flow Rate and Flux Distribution 61
4.3 Influence of Crushed Zone around Perforation Tunnel 65
4.3.1 Uniform Skin Distribution 66
4.3.2 Non-Uniform Skin Distribution 70
4.4 Effect of Test Configuration on Core Flow Efficiency 78
4.5 Impact of Variable Perforation Radius 82
4.6 Effect of Core Size on CFE 84
4.7 What to Make of CFE? 86
4.8 Criterion and Procedure to Rank Jet Perforators 91
4.9 Evaluation of the Hsia and Behrmann Equivalent Skin Equation 93
CHAPTER 5 CONCLUSIONS 96
NOMENCLATURE 99
REFERENCES 102
APPENDIX A COMPUTER CODES 105
A-1 Computer Code for Axial Flow Configuration 105
A-2 Computer Code for Semi-Radial Flow Configuration 109
A-3 Computer Code for Radial-Axial Flow Configuration 113

LIST OF FIGURES

Figure 1.1- A schematic of the flow test equipment 6
Figure 2.1- A schematic of the analytical model 17
Figure 2.2- A schematic of axial laboratory flow target 18
Figure 2.3- A schematic of semi-radial laboratory flow target 35
Figure 2.4- A schematic of radial-axial laboratory flow target 48
Figure 3.1- Comparison of the axial model with the models in the literature, axial flow configuration 55
Figure 3.2- Error analysis for Dogulu's finite difference model 56
Figure 3.3- Comparison of the radial-axial model with Deo et al. model 57
Figure 3.4- Comparison of the semi-radial model with the existing models.....59
Figure 4.1- Flow rate influenced by test configuration and perforation length.....63
Figure 4.2- The impact of test configuration on flux distribution along a 10-in. perforation.....64
Figure 4.3- The effect of uniform skin on the flow across an axial target.....67
Figure 4.4- Impact of uniform skin factor on flow rate - Semi-radial flow target.....68
Figure 4.5- Impact of uniform skin factor on flow rate – Radial-axial flow target.....69
Figure 4.6- The effect of skin factor on the flow distribution - Axial configuration.....71
Figure 4.7- Impact of perforation damage on the flux distribution - Semi-radial case.....72
Figure 4.8- Skin distribution effect on flux distribution – Radial-axial case.....73
Figure 4.9- The effect of non-uniform skin on flux distribution - Axial configuration.....75

Figure 4.10- The impact of non-uniform skin on flux distribution - Semi-radial case.....76

Figure 4.11- The impact of non-uniform skin on flux distribution - Radial-axial case.....77

Figure 4.12- The impact of test configuration on CFE 79

LIST OF TABLES

Table 4.1- Basic input data 61

Table 4.2- The effect of variable perforation radius on CFE.....83

Table 4.3- Influence of core radius on CFE.....85

Table 4.4- Effect of core length on CFE.....86

Table 4.5- Input data for perforated well.....89

Table 4.6- CFE and PR comparison 90

Table 4.7- Effect of shot density and phasing angle on well productivity ratio 90

Table 4.8- Error Analysis for the Hsia and Behrmann Equation, $k_r/k_x=1$ 94

Table 4.9 - Error Analysis for the Hsia and Behrmann Equation, $k_r/k_x=0.5$ 94

Table 4.10 - Error Analysis for the Hsia and Behrmann Equation, $k_r/k_x=0.1$ 95

ACKNOWLEDGEMENT

First, I thank God for giving me the strength, inspiration, and guidance to complete this work. I would like to thank to my advisor Dr. Turhan Yildiz for supervising this MS thesis. I also would like to express my genuine appreciation to Dr. Erdal Ozkan and Dr. Hossein Kazemi for serving on the thesis committee.

INTRODUCTION

Perforating is a common well completion method. In this procedure, the perforating gun punches through the casing and cement around the well in different patterns. Perforations serve as flow paths to transport the fluids from the formation. However, perforation does not necessarily make the fluid movement more efficient. In some applications, perforating may upset the well productivity. There are many factors controlling the effectiveness of the perforating. Some of the factors are the perforating gun type, gun size, reservoir physical characteristics, perforation geometry, and formation stress condition. Perforation changes the flow geometry around the wellbore. Around the perforation, fluid flow is three dimensional (3-D). The 3-D nature of the flow around the perforation tunnel makes the perforation design and flow modeling complicated. It is important to understand the fluid flow around the perforation. Many studies have focused on investigating the effect of flow configuration around the perforation on well productivity.

One of the important factors that control perforation geometry is the perforating gun itself. In order to evaluate the perforator performance, a standard procedure called the API Recommended Practice 43 was published by the American Petroleum Institute in 1962. The API procedure was revised in 1971 and then in 1991. In the 5^{th} edition of the API RP43 published in 1991, a more realistic procedure was designed by applying overburden, confining, and pore pressure on the core target. The final edition of the API procedure was published in 2000 and is known as the API RP 19B.

In the API RP 19B procedure, a cylindrically shaped core target is perforated with a single shaped charge. The diameter of the core should be greater than 4 inches. The core length is typically in the range of 12 to 15 inches. Once the perforator is fired and a

hollow tunnel created, several measurements are made. Typically, the length of the perforation, the diameter of the entrance hole, and changes in the perforation diameter along the perforation axis are recorded. Additionally, post-perforation flow tests are run on the perforated core target. These flow tests are conducted by circulating a single-phase liquid across the core target. Total pressure drop and flow rate are measured.

Post-perforation flow tests may be conducted in three different flow configurations; axial, semi-radial, and radial-axial. These three flow configurations are distinguished from each other based on the flow conditions at the external boundaries of the perforated core target. The three post-perforation flow geometries will be described in detail later in this text.

During perforating, high pressures are generated and the core target is exposed to a very high stress. Due to high stress encountered, an altered zone around the perforation tunnel is created. The altered zone typically suffers from reduced permeability and porosity. The altered zone around the perforation tunnel is known as the crushed zone. The permeability in the crushed zone may be as low as 5-10% of the original core permeability, and the thickness of the crushed zone is in the order of ½ in. The permeability impairment in the crushed zone may result in a large additional pressure drop during the post-perforation flow tests. The permeability reduction in the crushed zone around the perforation tunnel is analogous to the formation damage around the wells.

The impact of permeability damage in the crushed zone is quantified in terms of core flow efficiency (CFE). The core flow efficiency is the ratio of the actual post-perforation flow rate measured on the core to the theoretical ideal flow rate calculated from the mathematical models considering the post-perforation flow geometry. The measured flow rate is influenced by the formation damage due to perforating. The ideal flow rate is calculated without considering the effect of formation damage. Thus core flow efficiency is an important parameter ranking the shaped charges.

The flow geometries encountered in post-perforation flow tests are multidimensional and complex. Traditionally, numerical methods/simulators have been

used to calculate the ideal rates for the complicated post-perforation flow tests. As a matter of fact, the API recommends the use of finite element models for calculating ideal post-perforation flow rate.

This study presents three analytical solutions to predict the ideal rates for the complicated post-perforation flow configurations. The analytical models are coded in a FORTRAN environment. The proposed solutions are compared with the existing numerical models and verified. The analytical solutions are general, available to the public, and very fast and inexpensive to compute.

Using the analytical models, a sensitivity study investigating the effect of perforating parameters on the CFE has been conducted. It is demonstrated that the post-perforation flow geometry, core/perforation dimensions, permeability anisotropy, and the degree of formation damage control the CFE. It is shown that the same degree of formation damage yields different CFE in different post-perforation flow geometries. A method to convert the CFE data to an equivalent skin factor is presented. Finally, a procedure to rescale the skin factor from core targets to a perforated well is introduced.

CHAPTER 1

LITERATURE REVIEW

1.1 Introduction

A good perforation design can improve the well productivity significantly. In order to have a good and effective perforation design, the nature of the flow around the perforations under downhole conditions has to be understood very well. Since the invention of the perforating process, there have been many studies investigating different aspects of the perforating technology. The current literature spans from the recommended laboratory test procedures to the simulation of three dimensional flow into multiple perforations around the oil and gas wells. In this section, a brief summary of the previous research studies has been presented. Studies focusing on the flow around a single perforation in core targets, the productivity of perforated wells, and the API recommended testing procedure are reported.

1.2 API RP 19B

The API proposed a testing procedure and evaluation method to measure the relative merits of well perforators. The API procedure is titled "Recommended Practices for Evaluation of Well Perforators". The latest edition of the practice has been published in September 2001 and is known as the API Recommended Practice 19B. The procedure consists of four parts.

1. Evaluation of the perforation systems under surface conditions using concrete targets.
2. Evaluation of the perforators under stress conditions using Berea targets.
3. Evaluation of the perforator systems at elevated temperature conditions using steel targets.
4. Evaluation of the perforation flow performance under simulated downhole conditions.

This study focuses on the fourth part subtitled "Evaluation of Perforation Flow Performance under Simulated Downhole Conditions". The purpose of this part of the procedure is to provide a measure of flow performance of a single perforation.[1]

Fig.1.1 displays a schematic of the apparatus recommended by the API and is directly taken from Ref. 1. The apparatus consists of several vessels. Two of the main vessels are for simulating the wellbore and overburden pressure. The simulated wellbore vessel is charged with a pressure of 1,000 psi. The target core to be perforated is placed in the simulated overburden pressure vessel applying an external confining pressure of 4,500 psi on the core target. The simulated overburden pressure vessel is designed such that a single phase fluid (typically 3% sodium chloride brine solution) could be injected through the core target. During the perforating, the core possesses a pore pressure of 1,500 psi.

The target core is usually a sandstone outcrop (typically Berea). The target diameter has to be greater than 4 inches. Before perforating, the axial and diametric permeability of the core are measured. The rock sample placed in the pressure vessel is assembled with a faceplate, a flexible jacket, and a flow distributor. The faceplate simulates the casing. The flexible jacket transmits the simulated confining stress to the core target. The axial and radial stresses could differ; however, the confining stress has to be applied uniformly.

The perforating charge is placed in the wellbore vessel. The charge has to be taken directly from the manufacturing line. Additionally, the charges are aged for a minimum of four weeks prior to testing.

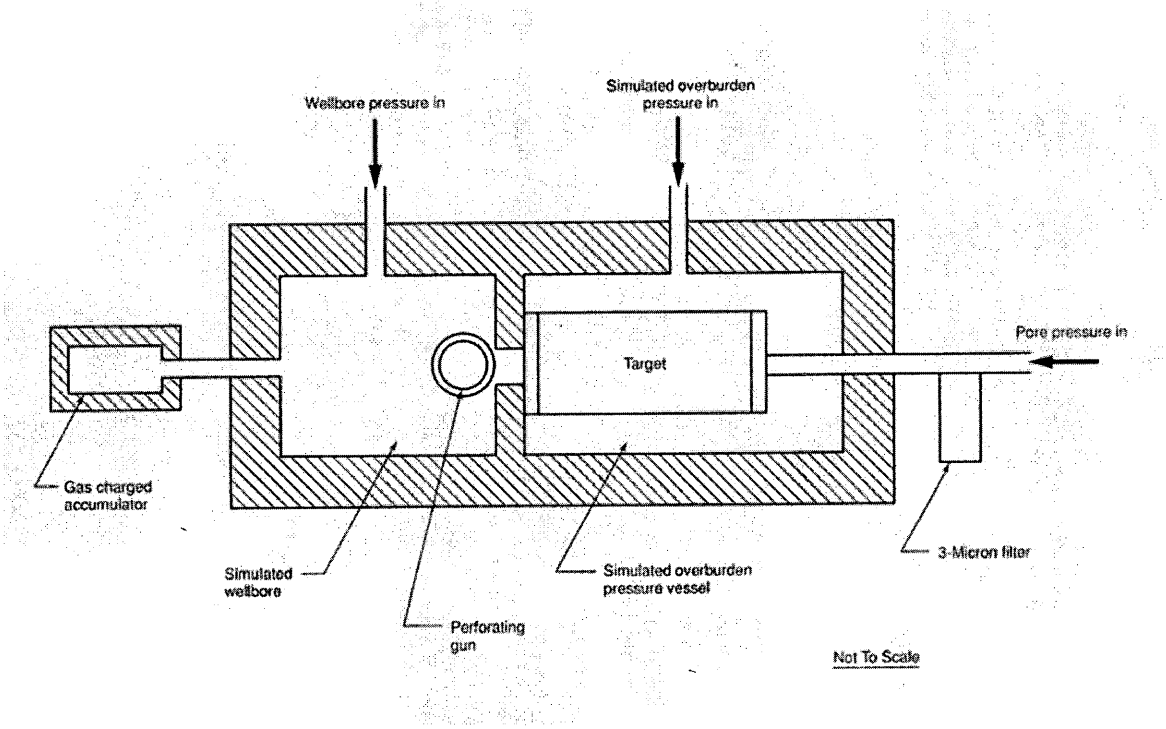

Figure 1.1- A schematic of the flow test equipment (Ref. 1).

After the charge is fired, wellbore/pore pressure may be gradually reduced to the ambient pressure if desired. However, the effective pressure, which is the confining pressure minus pore pressure, must be kept constant. After the charge is fired, several important parameters are measured.

In the next step, flow through the sample is initiated by applying pore pressure and post-perforation flow tests are conducted. Post-perforation flow tests may be run under three different types of external boundary conditions: semi-radial flow, axial flow, or radial-axial flow. The type of the external boundary condition determines how much the fluid needs to converge around the perforation. Pore pressure can be applied to the cylindrical sides of the core sample, un-perforated end of the core, or both the external cylindrical surface and un-perforated end of the core simultaneously. When only the external cylindrical surface is open to flow, semi-radial flow geometry is encountered. Axial flow configuration is set up by injecting the pore fluid at the un-perforated end of the core only. If both the cylindrical surface and un-perforated end of the core simultaneously admit pore fluid then, the radial-axial flow pattern is observed.

For each perforation test, the following data should be recorded.

1. A drawing of the test geometry and flow boundary conditions
2. Core sample source, diameter, length, orientation, and fluid saturation
3. Axial and diametric core permeability before perforating
4. Test conditions during shooting and flowing
5. Perforation geometry; total perforation length, debris-free length, and perforation diameter profile
6. Differential pressure and flow rate
7. Fluid inlet temperature and viscosity

The results from post-perforation tests are used to calculate the core flow efficiency (CFE). Perforating charge creates extremely high stress on the core sample and crushes the rock around the perforation tunnel. CFE is a measure of the permeability damage around the perforation tunnel. CFE is the ratio of the actual post-perforation flow rate measured on the core to the theoretical ideal flow rate calculated from the mathematical models considering post-perforation flow geometry. The measured flow

rate is influenced by the formation damage due to the perforating. The ideal flow rate is calculated without considering the effect of formation damage. Mathematically, CFE is defined as

$$\text{CFE} = \frac{q_m}{q_{ideal}} = \frac{\Delta p_{ideal}}{\Delta p_m} \tag{1.1}$$

where

q_m = Measured flow rate

q_{ideal} = Ideal flow rate

Δp_m = Measured pressure drop

Δp_{ideal} = Ideal pressure drop

The ideal flow rate considering post-perforation flow geometry is calculated using mathematical models. The API has recommended the use of the following equation to predict the ideal flow rates for the post-perforation flow tests with semi-radial and radial-axial geometry.

$$q_{ideal} = 1.08 \times 10^{-3} \frac{\Delta p_m}{\mu} \left[\frac{k_1 L_p}{\ln(r_c / r_p)} + \frac{k_2 r_p r_c}{r_c - r_p} \right] \tag{1.2}$$

where q_{ideal} and Δp_m are measured in cc/sec and psi, respectively. The rest of the parameters appearing in Eq. 1.2 are

μ = Viscosity, cp

L_p = Perforation length, in.

r_p = Perforation radius, in.

r_c = Core radius, in.

For cores oriented with axes parallel to bedding plane

$$k_1 = k_2 = \sqrt{k_\perp \, k_{//}} \tag{1.3}$$

For cores oriented with axis perpendicular to bedding

$$k_1 = k_{//} \tag{1.4}$$

$$k_2 = (k_\perp \, k_{//}^2)^{1/3} \tag{1.5}$$

where

$k_{//}$ = Permeability in the direction parallel to bedding plane

$k_\perp$ = Permeability in the direction perpendicular to bedding plane

It should be reminded again that the equations above are recommended only for the semi-radial and radial-axial configurations. In addition to the API equation, numerical methods/simulators have been used to calculate the ideal rates for the semi-radial and radial-axial configurations.

The API practice does not provide simple equations to estimate the ideal flow rate for the axial test apparatus. API recommends the use of finite element models for calculating the ideal post-perforation flow rate for the axial setup.

Traditionally, service companies use finite element or finite difference codes to calculate the ideal flow rate and the CFE.

1.3 Flow Models for Post-Perforation Flow Tests

To understand the flow performance around a single shot perforation on the API specified core targets, many different aspects of the process has been investigated experimentally. Additionally, numerical models conforming to the flow geometry of single shot perforation have been constructed to simulate the flow. Here, we present a brief summary of current literature.

In 1972, Bell et al.[2] developed a finite difference model to compute pressure and flow distribution for ideal perforation in linear laboratory flow targets. They also constructed a mathematical model for downhole flow conditions. They compared the results from the downhole model and the linear laboratory target. They concluded that the post-perforation flow tests conducted on the semi-radial setup represent downhole conditions much better than those run on the axial setup. Bell et al.[2] were the first, suggesting the use of radial flow concept to estimate the CFE. They also analyzed the effect of the crushed zone on flow distribution around the perforation tunnel.

In 1974, Klotz et al.[3] compared the flow on the linear core model for downhole conditions with realistic shot densities and phasing. They used an asymmetric 2-D model for the linear core target. Their downhole model considered a phasing angle of 90 degrees and a 4 shots per/ft shot density. They concluded that, in an ideal single perforation shot at the linear core targets, most of the flow is through the tip of the perforation and flux along a single perforation is nearly exponential in shape. However, in downhole conditions, the flow is evenly distributed along the perforation axis.

In 1978, Saucier and Lands[4] experimentally investigated the effect of stress conditions on the flow characteristics and the CFE of the perforated core targets.

In 1988, Regalbuto et al.[5] conducted an experimental study to investigate the effect of high differential pressure on the radial flow ratio (RFR) which is defined as the ratio of core flow rates before and after perforating. They applied three different levels of underbalance pressure across the perforated cores; no underbalance pressure, high underbalance pressure at the time of perforating, and high underbalance pressure applied after perforating. They observed that the experiments conducted with high differential pressure at the time of perforating resulted in the highest RFR. As expected, the experiments with zero underbalance showed the worst performance.

In 1988, Behrman and Halleck[6,7] presented the results from their experimental studies focusing on the effect of wellbore pressure on the perforation length and the impact of concrete and core rock strengths on the perforator performance.

In 1989, Doe et al.[8] developed different models to investigate the flow tests described in the API RP 43 and the flow into a perforated well. Using a commercially available finite element code developed for heat transfer applications, they analyzed the flux distribution along a single perforation under the axial and radial-axial test configurations. They also built a model for downhole conditions. They investigated the effect of shot density, perforation phasing angle, crushed zone characteristics, and wellbore damage on flow distributions in downhole conditions. Comparing the laboratory and downhole flow models, they concluded that neither axial nor radial-axial laboratory flow targets represent the flow in downhole conditions properly.

In 1989, Halleck and Deo[9] conducted experiments investigating the effect of the underbalance pressure on the flow characteristics of a single perforation.

The permeability impairment in the crushed zone around the perforation tunnels creates additional pressure drop. This effect is formulated in terms of a skin factor. The crushed zone skin factor has a tremendous effect on the productivity of the perforated core targets and well. Therefore, many studies[10-12] have been dedicated to sorting out the impact of the crushed zone skin factor. In 1991, Behrman et al. [10] experimentally measured the additional skin factor created during perforating. They used the

infinitesimally thin skin factor concept developed for vertical openholes. In the same year, Hsia and Behrman[11] ran experiments on two different types of sandstone cores to determine the underbalance pressure needed to eliminate the skin factor in the crushed zone. Also in 1991, Pucknell and Behrman[12] used the CAT scan technology to investigate the perforation crushed zone. They measured the crushed zone permeability using a mini-permeameter and radial flow permeameter. They concluded that, contrary to the claims in some earlier studies, the crushed zone around the perforation tunnel is not compacted.

In 1993, Behie and Settari[13] developed two new finite difference models to determine the productivity of the single perforation on core targets and multi-perforation systems around the wells. Their simulators could account for multi-phase flow effects. The single perforation model is designed to analyze the API tests on the core targets under laboratory conditions. Their single perforation model could automatically generate grids and three different boundary conditions, handle non-Darcy flow, and allow up to two conically shaped crushed zones. Their model requires a minimum of 1,320 grid blocks. They concluded that the API formulation to evaluate anisotropy effect in radial and axial flow configurations is incorrect. Besides the single perforation model for evaluating the post-perforation flow tests, Behie and Settari[13] built a three-dimensional multi-perforation model for the realistic wells in the field context. This model can be used for both vertical and horizontal wells.

In 1994, Rochon et al.[14] perforated several cores according to the API practice and proposed a testing method to estimate the damage around the perforation tunnel. They saturated the core with a low viscosity fluid then, after perforating, they flushed the low viscosity fluid with a more viscose fluid. By monitoring the differential pressure when viscose fluid moves forward in the core, they were able to predict the crushed zone thickness and the change in permeability in the crushed zone.

Using a 2D finite difference model, Dogulu[15] and Halleck and Dogulu[16] reviewed the API RP43 flow test and recommended some modifications to the procedure. Their numerical model could handle both the axial and radial-axial laboratory flow targets.

Additionally, they compared the 4th and 5th editions of the API RP 43 procedure. They also provided a procedure to relate the CFE obtained on the core targets to a skin value which can be used in conjunction with the productivity models for the perforated wells.

In 2000, Devinder and Sharma[17] built an experimental model to investigate the factors controlling the permeability distribution around a perforation tunnel.

In 2001, using the visualization technology, Halleck et al.[18] mapped the permeability profile around the perforations. They concluded that the permeability in the crushed zone varies gently along the perforation tunnel.

In 2002 Folse et al.[19] presented results from their experimental and modeling studies considering the API RP 43 procedure. The main objective in their study was to optimize the well inflow performance. They concluded that the actual well inflow performance in downhole conditions is different from the flow characteristics on both axial and radial flow configurations. They stated that scaling the lab results to downhole conditions is a challenging task.

1.4 Inflow Models for Perforated Wells

Post-perforation flow tests are run on a single perforation in a cylindrically shaped core target. This leads to a simplified flow geometry compared to the flow configuration around a perforated well. Therefore, it is necessary to differentiate between the flow into a single perforation in the core targets and that into multiple perforations around the completed wells. To understand the inflow performance of perforated wells, researchers built numerical models.[3,8,13,19,20,23] Besides the references cited here, there are many other numerical models available in the literature. It is impractical to list all the relevant studies. Below we briefly summarize some of the relevant works.

Tariq[20] built a finite element model for steady state flow into perforated completion. He used the same commercial simulator described by Deo et al. [8] The model

by Tariq[20] accounts for the non-Darcy flow in the formation. He concluded that the productivity ratio values reported for perforated wells in some of the earlier simulation studies were optimistic.

Using the same finite element based software, Karakas and Tariq[21] conducted an extensive simulation study. They investigated the effects of different perforation and reservoir parameters on the productivity of perforated completion. Based on the results from their extensive simulation study, they proposed a semi-analytical equation to predict the pseudoskin which is created due to perforating. Their perforation pseudoskin model is relatively simple and easy to use.

In 2000, Yildiz[22] developed a 3D analytical flow model to predict the productivity of selectively perforated wells. The 3D analytical flow model was compared against some of the existing numerical models as well as the experimental data obtained on electrolytic apparatus.

In 2002, Ansah et al.[23] built a new 3-D finite element wellbore inflow model. Their fine grid model uses 30,000 elements for each perforation. They concluded that, to predict the perforation flow performance accurately, the exact perforation geometry has to be well defined. They also investigated the effect of permeability anisotropy and verified the results previously presented by Tariq.

CHAPTER 2

POST-PERFORATION FLOW MODELS

2.1 Introduction

In this section, we present the analytical post-perforation flow models for axial, semi-radial, and radial-axial core setups. Single phase flow of a slightly compressible fluid under steady state conditions is considered. In all three configurations, the 2-D diffusivity equation in radial coordinate system (r-x) governs the flow process.

The perforation is divided into N number of smaller segments in all three models. A variable perforation radius and a non-uniform damage along the perforation axis may be assigned. It is assumed that the pressure loss inside the perforation tunnel is negligible; i.e., infinite-conductivity condition prevails. The flux along a given segment is uniform. However, flux along the perforation tunnel varies in a staircase fashion.

In the model development, it is assumed that the pressure drop across the perforated core is the measured parameter, and the ideal flow rate is the calculated quantity. The solutions are casted in such a way that the total flow rate and flow distribution along the perforation are all calculated for a given total pressure drop across the core target.

The general stepwise algorithm below is followed to find all three solutions.

- Divide the perforation into N number of segments.
- Write down the differential equation and boundary conditions.
- Apply the method of separation of variables. This technique gives the solution in the form of a Fourier series.

- Use the theory of Fourier series expansion to reach the final solution for pressure drop anywhere in the perforated core.
- Evaluate the general pressure drop solution at the jth perforation segment.
- Use the pressure-averaging method to have a constant pressure drop along the jth perforation segment.
- Incorporate the effect of formation damage in the form of a variable skin factor.
- Write the solution for all the segments. At this point, the pressure drops in all the segments are formulated.
- Impose an infinite-conductivity condition inside the perforation. The infinite-conductivity condition requires pressure drop at each perforation segment be the same and equal to the pressure drop across the perforated core target. This results in N number of pressure drop equations.
- Combine the rate equation with the pressure equations. The rate equation is based on the fact that the sum of the individual segment flow rates is equal to the total flow rate across the core target. This results in (N+1) equation with (N+1) unknowns.
- Recast the (N+1) equations in a matrix form. Solve the matrix for the total flow rate and segment rate distribution.

Below, we present the details of the mathematical procedures used to find the post perforation flow models. Fig. 2.1 shows a schematic of the analytical model.

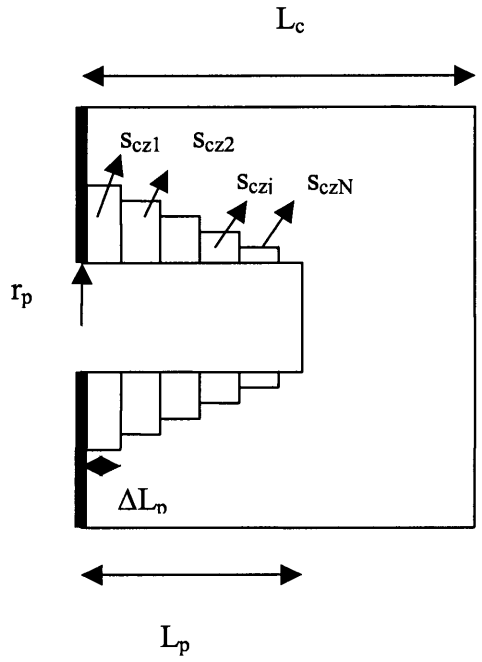

Figure 2.1- A schematic of the analytical model.

2.2 Model for Axial Laboratory Flow Target

In the axial flow configuration case, the fluid is injected from the un-perforated end of the core and all other boundaries are sealed. Fig. 2.2 shows a schematic of the boundary conditions prevailing on an axial laboratory flow target. Mathematical procedure to build the model for the axial laboratory flow target is as follows. The 2-D diffusivity equation in the radial coordinate system governs the flow.

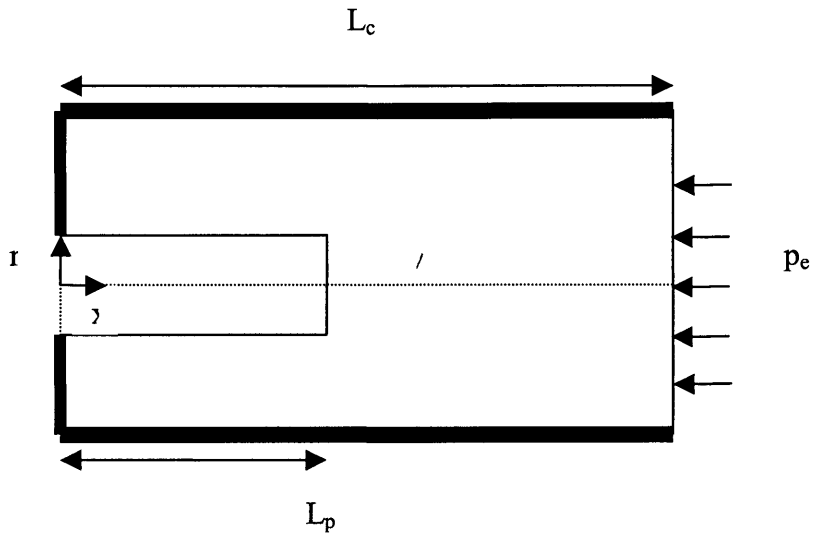

Figure 2.2 - A schematic of axial laboratory flow target.

$$\frac{\partial^2(\Delta p)}{\partial r^2}+\frac{1}{r}\frac{\partial(\Delta p)}{\partial r}+\frac{k_x}{k_r}\frac{\partial^2(\Delta p)}{\partial x^2}=0 \tag{2.1}$$

where

$$\Delta p(r,x)=p_e-p(r,x) \tag{2.2}$$

The boundary conditions for axial flow geometry are

$$1.\ \left(r\frac{\partial(\Delta p)}{\partial r}\right)_{r=r_p} = -\sum_{i=1}^{N}\{H[x-(i-1)\Delta L_{pi}]-H[x-i\Delta L_{pi}]\}\frac{q_i\,\mu}{2\pi\,\alpha\,k_r\,\Delta L_{pi}} = G(x) \quad (2.3)$$

$$2.\ \frac{\partial(\Delta p)}{\partial r}\Big|_{r=r_e} = 0 \quad (2.4)$$

$$3.\ \Delta p(r, L_c) = 0 \quad (2.5)$$

$$4.\ \frac{\partial(\Delta p)}{\partial x}\Big|_{x=0} = 0 \quad (2.6)$$

where α is the unit conversion factor. $\alpha = 1.127\times10^{-3}$ and $\alpha = 1$ is for the field and cgs units, respectively.

The boundary value problem defined in Eqs. 2.1 through 2.6 could be solved using the method of separation of variables.

$$\Delta p(r,x) = R(r)X(x) \quad (2.7)$$

where $R(r) \neq 0$ and $X(x) \neq 0$.

Evaluating the first and second order partial derivates

$$\frac{\partial(\Delta p)}{\partial r} = R'(r)X(x) \quad (2.8)$$

$$\frac{\partial^2(\Delta p)}{\partial r^2} = R''(r)X(x) \quad (2.9)$$

$$\frac{\partial(\Delta p)}{\partial x} = R(r)X'(x) \tag{2.10}$$

$$\frac{\partial^2(\Delta p)}{\partial x^2} = R(r)X''(x) \tag{2.11}$$

Substituting Eqs. 2.9 and 2.11 into the governing differential equation,

$$R''(r)X(x) + \frac{1}{r}R'(r)X(x) + \frac{k_x}{k_r}R(r)X''(x) = 0 \tag{2.12}$$

Dividing all terms in Eq. 2.12 by $R(r)X(x)$

$$\frac{R''}{R} + \frac{1}{r}\frac{R'}{R} + \frac{k_x}{k_r}\frac{X''}{X} = 0 \tag{2.13}$$

Rearranging Eq. 2.13

$$\frac{R''}{R} + \frac{1}{r}\frac{R'}{R} = -\frac{k_x}{k_r}\frac{X''}{X} = \beta = \text{Constant} \tag{2.14}$$

Eq. 2.14 yields two separable ordinary differential equations.

$$r^2R'' + rR' - \beta r^2 R = 0 \tag{2.15}$$

$$X'' + \beta \frac{k_r}{k_x} X = 0 \tag{2.16}$$

Now, we apply the separation of variables to the homogenous boundary conditions.

$$2.\quad \frac{\partial(\Delta p)}{\partial r}\Big|_{r=r_e} = 0 \quad \rightarrow \quad R'(r_e)X(x) = 0 \quad \rightarrow \quad R'(r_e) = 0 \tag{2.17}$$

$$3.\quad \Delta p(r, L_c) = 0 \quad \rightarrow \quad R(r)X(L_c) = 0 \quad \rightarrow \quad X(L_c) = 0 \tag{2.18}$$

$$4.\quad \frac{\partial(\Delta p)}{\partial x}\Big|_{x=0} = 0 \quad \rightarrow \quad R(r)X'(0) = 0 \quad \rightarrow \quad X'(0) = 0 \tag{2.19}$$

The separation constant β may be zero, positive or negative. Now, we solve the ordinary differential equations given in Eqs. 2.15 and 2.16

2.2.1 Case 1; $\beta = 0$

For $\beta = 0$, the ordinary differential equation given in Eq. 2.16 is reduced to

$$X''(x) = 0 \tag{2.20}$$

The solution to Eq. 2.20 is

$$X'(x) = a_1 \tag{2.21}$$

$$X(x) = a_1 x + a_2 \tag{2.22}$$

Using the fourth boundary condition

$$X'(0) = a_1 = 0 \quad \rightarrow \quad a_1 = 0 \tag{2.23}$$

Using the third boundary condition

$$X(L_c) = a_2 = 0 \quad \rightarrow \quad a_2 = 0 \tag{2.24}$$

$\beta = 0$ yields trivial solution of $X(x) = 0$. $\beta = 0$ case cannot be a valid solution, hence, it is eliminated.

2.2.2 Case 2; $\beta = -\lambda^2 < 0$

For $\beta = -\lambda^2 < 0$, Eq. 2.16 becomes

$$X'' - \lambda^2 \frac{k_r}{k_z} X = 0 \tag{2.25}$$

The general solution to Eq. 2.25 is

$$X(x) = a_3 \cosh(\lambda \sqrt{k_r / k_x}\, x) + a_4 \sinh(\lambda \sqrt{k_r / k_x}\, x) \tag{2.26}$$

Taking the derivative of Eq. 2.26

$$X'(x) = a_3 \lambda\sqrt{k_r/k_x}\sinh(\lambda\sqrt{k_r/k_x}x) + a_4 \lambda\sqrt{k_r/k_x}\cosh(\lambda\sqrt{k_r/k_x}x) \qquad (2.27)$$

Using the fourth boundary condition

$$X'(0) = 0 + a_4 \lambda\sqrt{k_r/k_x} = 0 \quad \rightarrow \quad a_4 = 0 \qquad (2.28)$$

Using the third boundary condition

$$X(L_c) = a_3 \cosh(\lambda L_c \sqrt{k_r/k_x}) = 0 \qquad (2.29)$$

For Eq. 2.29 to hold, either $a_3 = 0$ or $\cosh(\lambda L_c \sqrt{k_r/k_x}) = 0$. Since $\cosh(x)$ is never zero, a_3 must be equal to zero; $a_3 = 0$. Therefore, $\beta = -\lambda^2 < 0$ yields trivial solution.

2.2.3 Case 3; $\beta = \lambda^2 > 0$

For $\beta = \lambda^2 > 0$, Eq. 2.16 is

$$X'' + \frac{k_r}{k_x}\lambda^2 X = 0 \qquad (2.30)$$

The general solution of Eq. 2.30 is

$$X(x) = a_5 \cos(\lambda\sqrt{k_r/k_x}x) + a_6 \sin(\lambda\sqrt{k_r/k_x}x) \qquad (2.31)$$

Taking the derivative of Eq. 2.31, we have

$$X'(x) = -a_5 \lambda \sqrt{k_r/k_x} \sin(\lambda \sqrt{k_r/k_x}\, x) + a_6 \lambda \sqrt{k_r/k_x} \cos(\lambda \sqrt{k_r/k_x}\, x) \qquad (2.32)$$

Applying the fourth boundary condition

$$X'(0) = 0 + a_6 \lambda \sqrt{k_r/k_x} = 0 \quad \rightarrow \quad a_6 = 0 \qquad (2.33)$$

Using the third boundary condition

$$X(L_c) = a_5 \cos(\lambda L_c \sqrt{k_r/k_x}) = 0 \qquad (2.34)$$

To satisfy Eq. 2.34, either $a_5 = 0$ or $\cos(\lambda L_c \sqrt{k_r/k_x}) = 0$. The choice $a_5 = 0$ leads to trivial solution. Hence, we chose the second case. The expression $\cos(\lambda L_c \sqrt{k_r/k_x}) = 0$ is satisfied when $\lambda L_c \sqrt{k_r/k_x} = \frac{(2n-1)}{2}\pi$, where n=1,2,3,..... This leads to

$$\lambda_n = \frac{(2n-1)\pi}{2L_c} \sqrt{k_x/k_r} \qquad n = 1,2,3,..... \qquad (2.35)$$

where $\lambda_n's$ are the eigenvalues. The eigenfunctions corresponding to the eigenvalues given in Eq. 2.35 is

$$X_n(x) = a_n \cos(\lambda_n \sqrt{k_r/k_x}\, x) = a_n \cos\left[\frac{(2n-1)\pi x}{2L_c}\right] \tag{2.36}$$

We end up with an infinite number of solutions to Eq. 2.16. Now, we search for the solution to Eq. 2.15. For $\beta = \lambda^2 > 0$, Eq. 2.15 becomes

$$r^2 R_n'' + r R_n' - r^2 \lambda_n{}^2 R_n = 0 \tag{2.37}$$

Eq. 2.37 is the zero order modified Bessel differential equation. The general solution for this ordinary differential equation is as follows.

$$R_n(r) = A_n I_0(\lambda_n r) + B_n K_0(\lambda_n r) \tag{2.38}$$

Taking the derivative of Eq. 2.38 with respect to r

$$R_n'(r) = A_n \lambda_n I_1(\lambda_n r) - B_n \lambda_n K_1(\lambda_n r) \tag{2.39}$$

Applying the second boundary condition

$$R_n'(r_e) = A_n \lambda_n I_1(\lambda_n r_e) - B_n \lambda_n K_1(\lambda_n r_e) = 0 \tag{2.40}$$

Rearranging Eq. 2.40 for B_n

$$B_n = A_n \frac{I_1(\lambda_n r_e)}{K_1(\lambda_n r_e)} \tag{2.41}$$

Substituting Eq. 2.41 into Eq. 2.38,

$$R_n(r) = A_n\, I_0(\lambda_n r) + A_n \frac{I_1(\lambda_n r_e)}{K_1(\lambda_n r_e)} K_0(\lambda_n r) = A_n\, I_1(\lambda_n r_e)\left[\frac{I_0(\lambda_n r)}{I_1(\lambda_n r_e)} + \frac{K_0(\lambda_n r)}{K_1(\lambda_n r_e)}\right] \tag{2.42}$$

Multiplication of the functions $R_n(r)$ and $X_n(x)$ results in

$$\Delta p_n(r,x) = A_n\, a_n\, I_1(\lambda_n r_e)\left[\frac{I_0(\lambda_n r)}{I_1(\lambda_n r_e)} + \frac{K_0(\lambda_n r)}{K_1(\lambda_n r_e)}\right]\cos\left[\frac{(2n-1)\pi x}{2\,L_c}\right]$$

$$= F_n\, I_1(\lambda_n r_e)\left[\frac{I_0(\lambda_n r)}{I_1(\lambda_n r_e)} + \frac{K_0(\lambda_n r)}{K_1(\lambda_n r_e)}\right]\cos\left[\frac{(2n-1)\,\pi x}{2\,L_c}\right] \tag{2.43}$$

Now, we have infinite number of functions satisfying the boundary value problem described in Eqs. 2.1 through 2.6. To obtain the complete and unique solution, the superposition theorem is used.

$$\Delta p(r,x) = \Delta p_1(r,x) + \Delta p_2(r,x) + ... + \Delta p_n(r,x) + ... = \sum_{n=1}^{\infty} \Delta p_n(r,x) \tag{2.44}$$

$$\Delta p(r,x) = \sum_{n=1}^{\infty} F_n\, I_1(\lambda_n r_e)\left[\frac{I_0(\lambda_n r)}{I_1(\lambda_n r_e)} + \frac{K_0(\lambda_n r)}{K_1(\lambda_n r_e)}\right]\cos\left[\frac{(2n-1)\,\pi x}{2\,L_c}\right] \tag{2.45}$$

To find out what F_n is, the first boundary condition is used. Taking the derivative of Eq. 2.45 with respect to r,

$$\Delta p'(r,x) = \sum_{n=1}^{\infty} F_n \lambda_n I_1(\lambda_n r_e)\left[\frac{I_1(\lambda_n r)}{I_1(\lambda_n r_e)} - \frac{K_1(\lambda_n r)}{K_1(\lambda_n r_e)}\right]\cos\left[\frac{(2n-1)\pi x}{2L_c}\right] \tag{2.46}$$

If we evaluate the pressure derivative at the perforation radius the first boundary condition becomes

$$r_p \frac{\partial \Delta p}{\partial r}\Big|_{r=r_p} = r_p \sum_{n=1}^{\infty} F_n \lambda_n I_1'(\lambda_n r_e)\Omega_{an}(r_p)\cos\left[\frac{(2n-1)\pi x}{2L_c}\right] = G(x) \tag{2.47}$$

where $G(x)$ is given in Eq. 2.3 and $\Omega_{an}(r_p)$ is

$$\Omega_{an}(r_p) = \frac{I_1(\lambda_n r_p)}{I_1(\lambda_n r_e)} - \frac{K_0(\lambda_n r_p)}{K_1(\lambda_n r_e)} \tag{2.48}$$

Examination of Eq. 2.47 reveals that the expression in Eq. 2.47 can be considered as a Fourier Series expansion of the function $G(x)$.

To determine F_n constant, we multiply Eq. 2.47 by the term $\cos\left[\frac{(2m-1)\pi x}{2L_c}\right]$ and integrate the resulting expression in $0 \le x \le L_c$.

$$r_p \sum_{n=1}^{\infty} F_n \lambda_n I_1(\lambda_n r_e)\Omega_{an}(r_p) \int_0^{L_c} \cos\left[\frac{(2n-1)\pi x}{2L_c}\right] \cos\left[\frac{(2m-1)\pi x}{2L_c}\right] dx =$$

$$= \int_0^{L_c} G(x) \cos\left[\frac{(2m-1)\pi x}{2L_c}\right] dx \tag{2.49}$$

Now, we evaluate the integrals in Eq. 2.49 for $n = m$.

$$\int_0^{L_c} \cos\left[\frac{(2n-1)\pi x}{2L_c}\right] \cos\left[\frac{(2m-1)\pi x}{2L_c}\right] dx = 0 \tag{2.50}$$

When $n \neq m$

$$\int_0^{L_c} \cos\left[\frac{(2n-1)\pi x}{2L_c}\right] \cos\left[\frac{(2m-1)\pi x}{2L_c}\right] dx = \frac{L_c}{2} \tag{2.51}$$

The integral on the right hand side of the Eq. 2.49 is evaluated as shown bellow.

$$\int_0^{L_c} G(x) \cos\left[\frac{(2m-1)\pi x}{2L_c}\right] dx = \int_0^{L_c} G(x) \cos\left[\frac{(2n-1)\pi x}{2L_c}\right] dx$$

$$= \frac{-\mu}{2\pi\alpha k_r} \sum_{i=1}^{N} \int_0^{L_c} \frac{q_i}{\Delta L_{pi}} \left\{H\left[x-(i-1)\Delta L_{pi}\right] - H\left[x-i\Delta L_{pi}\right]\right\} \cos\left[\frac{(2n-1)\pi x}{2L_c}\right] dx$$

$$= \frac{-\mu}{2\pi\alpha k_r} \sum_{i=1}^{N} \frac{q_i}{\Delta L_{pi}} \int_{(i-1)\Delta L_{pi}}^{i\Delta L_{pi}} \cos\left[\frac{(2n-1)\pi x}{2L_c}\right] dx \tag{2.52}$$

The integral in Eq. 2.52 could be easily evaluated as shown below.

$$\int_{(i-1)\Delta L_{pi}}^{i\Delta L_{pi}} \cos\left[\frac{(2n-1)\pi x}{2L_c}\right] dx = \frac{2L_c}{(2n-1)\pi} R_{ani} \tag{2.53}$$

where

$$R_{ani} = \sin\left[\frac{(2n-1)\,\pi\, i\;\Delta L_{pi}}{2\,L_c}\right] - \sin\left[\frac{(2n-1)\,\pi\,(i-1)\;\Delta L_{pi}}{2\,L_c}\right] \tag{2.54}$$

Substituting Eqs. 2.53 and 2.54 into Eq. 2.52, we obtain

$$\int_0^{L_c} G(x)\ \cos\left[\frac{(2n-1)\pi x}{2L_c}\right] dx = \frac{-\mu}{2\pi\alpha k_r}\frac{2L_c}{(2n-1)\pi}\sum_{i=1}^{N}\frac{q_i}{\Delta L_{pi}}R_{ani} \tag{2.55}$$

Substituting Eqs. 2.50, 2.51 and 2.55 into Eq. 2.49,

$$r_p F_n \lambda_n I_1(\lambda_n r_e)\Omega_{an}\frac{L_c}{2} = \frac{-\mu}{2\pi\alpha k_r}\frac{2L_c}{(2n-1)\pi}\sum_{i=1}^{N}\frac{q_i}{\Delta L_{pi}}R_{ani} \tag{2.56}$$

Rearranging Eq.2.56 for F_n

$$F_n = -\frac{4\mu}{2\pi\alpha k_r r_p \pi}\frac{1}{\lambda_n(2n-1)I_1(\lambda_n r_e)\Omega_{an}(r_p)}\sum_{i=1}^{N}\frac{q_i}{\Delta L_{pi}}R_{ani} \tag{2.57}$$

Inserting the value of the eigenfunction (Eq. 2.35) into Eq. 2.57, we obtain

$$F_n = -\frac{8\mu L_c}{2\pi\alpha k_r r_p \pi^2\sqrt{k_x/k_r}}\sum_{i=1}^{N}\frac{q_i}{\Delta L_{pi}}\frac{1}{(2n-1)^2}\frac{R_{ani}}{I_1(\lambda_n r_e)\Omega_{an}(r_p)} \tag{2.58}$$

Substituting Eq. 2.58 into Eq. 2.45,

$$\Delta p(r,x) = \frac{8\mu L_c}{2\pi\alpha\sqrt{k_r k_x}}\frac{1}{r_p\pi^2}\sum_{i=1}^{N}\frac{q_i}{\Delta L_{pi}}\sum_{n=1}^{\infty}\frac{1}{(2n-1)^2}\psi_{an}(r)R_{ani}\cos\left[\frac{(2n-1)\pi x}{2L_c}\right] \tag{2.59}$$

$$\psi_{an}(r)=\frac{\frac{I_0(\lambda_n r)}{I_1(\lambda_n r_e)}+\frac{K_0(\lambda_n r)}{K_1(\lambda_n r_e)}}{-\frac{I_1(\lambda_n r_p)}{I_1(\lambda_n r_e)}+\frac{K_1(\lambda_n r_p)}{K_1(\lambda_n r_e)}} \tag{2.60}$$

Now, we evaluate the solution given in Eq. 2.59 at the sandface of the jth perforation segment.

$$\Delta p_{pj}(r_{pj},x)=\frac{8L_c}{\pi^2}\frac{\mu}{2\pi\alpha r_p\sqrt{k_x k_r}}\sum_{i=1}^{N}\frac{q_i}{\Delta L_{pi}}\sum_{n=1}^{\infty}\frac{1}{(2n-1)^2}\psi_{anj}(r_{pj})R_{ani}\cos\left[\frac{(2n-1)\pi x}{2L_c}\right] \tag{2.61}$$

where,

$$\psi_{anj}(r_{pj})=\frac{\frac{I_0(\lambda_n r_{pj})}{I_1(\lambda_n r_e)}+\frac{K_0(\lambda_n r_{pj})}{K_1(\lambda_n r_e)}}{-\frac{I_1(\lambda_n r_p)}{I_1(\lambda_n r_e)}+\frac{K_1(\lambda_n r_p)}{K_1(\lambda_n r_e)}} \tag{2.62}$$

Notice that the solution given in Eq. 2.61 yields a variable pressure along the perforation segment j. This is due to the uniform-flux assumption along a given single segment. To compensate for the variable pressure along a segment, we use the pressure averaging method.

$$\Delta\tilde{p}_{pj}=\frac{1}{\Delta L_{pj}}\int_{(j-1)\Delta L_P}^{j\Delta L_P}\Delta p_{pj}(x)dx \tag{2.63}$$

Substituting Eq. 2.61 into Eq. 2.63

$$\Delta\tilde{p}_{pj} = \frac{\mu}{2\pi\alpha r_p\sqrt{k_r k_x}}\frac{8L_c}{\pi^2}\sum_{i=1}^{N}\frac{q_i}{\Delta L_{pi}\Delta L_{pj}}\sum_{n=1}^{\infty}\frac{1}{(2n-1)^2}\psi_{anj}(r_{pj})R_{ani}\int_{(j-1)\Delta L_P}^{j\Delta L_P}\cos\left[\frac{(2n-1)\pi x}{2L_c}\right]dx \tag{2.64}$$

Evaluating the integral in Eq. 2.64

$$\int_{(j-1)\Delta L_P}^{j\Delta L_P}\cos\left[\frac{(2n-1)\pi x}{2L_c}\right]dx = \frac{2L_c}{(2n-1)\pi}R_{anj} \tag{2.65}$$

The pressure drop at the jth perforation segment could be obtained by substituting Eq. 2.65 into Eq. 2.64.

$$\Delta\tilde{p}_{pj} = \frac{\mu}{2\pi\alpha r_p\sqrt{k_r k_x}}\frac{16L_c^2}{\pi^3}\sum_{i=1}^{N}\frac{q_i}{\Delta L_{pi}\Delta L_{pj}}\sum_{n=1}^{\infty}\frac{\psi_{nj}(r_{pj})}{(2n-1)^3}R_{ani}R_{anj} \tag{2.66}$$

Pressure drop calculated in Eq. 2.66 is the ideal pressure drop, which assumes there is no crushed zone skin around the perforation tunnel. To account for the skin factor around each perforation segment, we assume that the flow across the damaged zone is normal to the perforation axis. The skin factor due to rock compaction in the crushed zone around the jth perforation segment is defined as

$$s_{czj} = \left(\frac{k_r}{k_{czj}} - 1\right)\ln\left(\frac{r_{czj}}{r_{pj}}\right) \tag{2.67}$$

where s_{czj} = skin factor around jth segment

k_{czj} = permeability in the crushed zone around the jth segment

r_{czj} = radius of the crushed zone around the jth segment

r_{pj} = radius of the jth perforation segment

The additional pressure drop because of the crushed zone around the jth perforation segment could be predicted as below.

$$\Delta p_{sj} = \frac{q_j \mu}{2\pi \alpha \Delta L_{pj} k_r} s_{czj} \tag{2.68}$$

The total pressure drop along the jth perforation segment is

$$\Delta p_{tj} = \Delta \tilde{p}_{pj} + \Delta p_{sj} \tag{2.69}$$

Substituting Eqs. 2.66 and 2.68 into 2.69

$$\Delta p_{tj} = \frac{\mu}{2\pi \alpha r_p \sqrt{k_r k_x}} \frac{16 L_c^2}{\pi^3} \frac{1}{\Delta L_{pi} \Delta L_{pj}} \sum_{n=1}^{\infty} \frac{1}{(2n-1)^3} \psi_{anj}(r_{pj}) R_{ani} R_{anj} + \frac{q_j \mu}{2\pi \alpha k_r \Delta L_{pj}} s_{czj} \tag{2.70}$$

Eq. 2.70 may be simplified as shown bellow

$$\Delta p_{tj} = \sum_{i=1}^{N} q_i B_{ji} \tag{2.71}$$

where

$$B_{ji} = \frac{\mu}{2\pi \alpha r_p \sqrt{k_r k_x}} \frac{16 L_c^2}{\pi^3} \frac{1}{\Delta L_{pi} \Delta L_{pj}} \sum_{n=1}^{\infty} \frac{1}{(2n-1)^3} \psi_{anj}(r_{pj}) R_{ani} R_{anj} \tag{2.72}$$

$$B_{jj} = \frac{\mu}{2\pi\alpha r_p \sqrt{k_r k_x}} \frac{16L_c^2}{\pi^3} \frac{1}{\Delta L_{pi} \Delta L_{pj}} \sum_{n=1}^{\infty} \frac{1}{(2n-1)^3} \psi_{anj}(r_{pj}) R_{ani} R_{anj} + \frac{\mu}{2\pi\alpha \Delta L_{pi} k_r} s_{czj} \tag{2.73}$$

At this point, we assume infinite-conductivity flow condition inside the perforation. Under infinite-conductivity assumption, there is no pressure loss inside the perforation. Therefore, the pressure drop at each perforation segment is the same and equal to total pressure drop across the perforation core target.

$$\Delta p_{t1} = \Delta p_{t2} = \Delta p_{t3} = ... = \Delta p_{tj} = ... = \Delta p_{tN} = \Delta p_{tm} \tag{2.74}$$

where, Δp_{tm} = total pressure drop measured across the perforated core.

Now, we rewrite Eq. 2.71 for all the segments and require that the pressure drop at each segment be equal to total pressure drop measured.

j=1 $$\Delta p_{t1} = \sum_{i=1}^{N} q_i B_{1i} = \Delta p_{tm} \tag{2.75}$$

j=2 $$\Delta p_{t2} = \sum_{i=1}^{N} q_i B_{2i} = \Delta p_{tm} \tag{2.76}$$

j=3 $$\Delta p_{t3} = \sum_{i=1}^{N} q_i B_{3i} = \Delta p_{tm} \tag{2.77}$$

$$\text{j=N-1} \quad \Delta p_{t(N-1)} = \sum_{i=1}^{N} q_i B_{(N-1)i} = \Delta p_{tm} \tag{2.78}$$

$$\text{j=N} \quad \Delta p_{tN} = \sum_{i=1}^{N} q_i B_{Ni} = \Delta p_{tm} \tag{2.79}$$

The linear system of equations described in Eqs. 2.75 through 2.79 result in N equations with (N+1) unknown. One more equation is needed to find the solution. The additional equation is obtained from the fact that the sum of the segment flow rates has to be equal to the total flow rate across the perforated core.

$$q_t = \sum_{i=1}^{N} q_i \quad \rightarrow \quad q_t - \sum_{i=1}^{N} q_i = 0 \tag{2.80}$$

The pressure drop equations (Eqs. 2.75 through 2.79) and rate equation (Eq. 2.80) may all be combined in a matrix format as shown bellow.

$$\begin{bmatrix} 1 & -1 & -1 & . & . & . & -1 \\ 0 & B_{11} & B_{12} & . & . & . & B_{1N} \\ 0 & B_{21} & B_{22} & . & . & . & B_{2N} \\ 0 & B_{31} & B_{32} & . & . & . & B_{3N} \\ . & . & . & & & & . \\ . & . & . & & & & . \\ . & . & . & & & & . \\ 0 & B_{N1} & B_{N2} & . & . & . & B_{NN} \end{bmatrix} \begin{bmatrix} q_t \\ q_1 \\ q_2 \\ q_3 \\ \\ \\ q_{N-1} \\ q_N \end{bmatrix} = \begin{bmatrix} 0 \\ \Delta p_{tm} \\ \Delta p_{tm} \\ \Delta p_{tm} \\ \\ \\ \Delta p_{tm} \\ \Delta p_{tm} \end{bmatrix} \tag{2.81}$$

The solution of Eq. 2.81 yields the total flow rate and flow rate of each perforation segment. The computer codes given by Press et al.[24] were used to solve the matrix presented in Eq. 2.81.

2.3 Model for Semi-Radial Laboratory Flow Target

In this case, fluid is injected from the cylindrical surface of the core and the un-perforated end of the core is sealed. Fig. 2.3 is a schematic of the boundary conditions in semi-radial laboratory flow target.

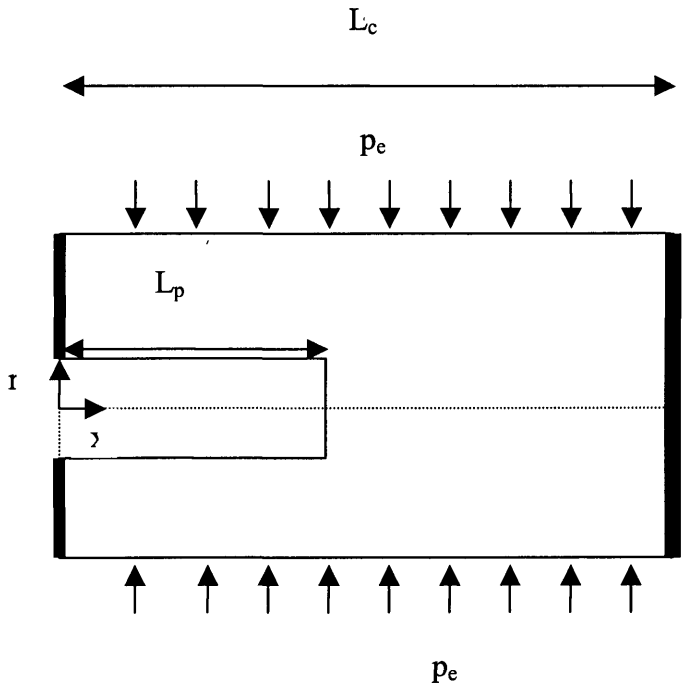

Figure 2.3 - A schematic of semi-radial laboratory flow target.

Single-phase fluid flow in semi-radial flow conditions is still governed by the diffusivity equation (Eq. 2.1). Additionally, two of the boundary conditions (first and fourth) are the same for both axial and semi-radial flow configurations. The boundary conditions expressed in Eqs. 2.3 and 2.6 hold for the flow in semi-radial flow configuration. The boundary conditions existing at $r = r_e$ and $x = L_c$ on the semi-radial geometry are different from those on axial geometry. The second and third boundary conditions for semi-radial geometry are

$$2.\ \Delta p(r_e, x) = 0 \tag{2.82}$$

$$3.\ \frac{\partial(\Delta p)}{\partial x}\Big|_{x=L_c} = 0 \tag{2.83}$$

To find a post-perforation flow model for the semi-radial geometry, we use the separation of variables as before. Application of separation of variables to Eq. 2.1 still leads to the ordinary differential equations given in Eqs. 2.15 and 2.16. Separation of variables applied to the fourth boundary condition leads to $X'(0) = 0$. In other words Eq. 2.19 still applies.

Applying the separation of variables to the second and third boundary conditions given in Eqs. 2.82 and 2.83, we obtain

$$2.\ \Delta p(r_e, x) = 0 \ \rightarrow\ R(r_e)X(x) = 0 \ \rightarrow\ R(r_e) = 0 \tag{2.84}$$

$$3.\ \frac{\partial(\Delta p)}{\partial x}\Big|_{x=L_c} = 0 \ \rightarrow\ R(r)X'(L_c) = 0 \ \rightarrow\ X'(L_c) = 0 \tag{2.85}$$

Now, we search for solutions corresponding three different cases of $\beta = 0$, $\beta = -\lambda^2 < 0$, and $\beta = \lambda^2 > 0$.

2.3.1 Case 1; $\beta = 0$

For $\beta = 0$, Eq. 2.16 reduces to

$$X_0''(x) = 0 \tag{2.86}$$

The general solution to Eq. 2.86 is

$$X_0'(x) = a_1 \tag{2.87}$$

$$X_0(x) = a_1 x + a_2 \tag{2.88}$$

Using the fourth boundary condition ($X_0'(0) = 0$), we have

$$X_0' = a_1 = 0 \quad \rightarrow \quad a_1 = 0 \tag{2.89}$$

The third boundary condition also verifies the results shown in Eq. 2.89. For $\beta = 0$, we have

$$X(x) = a_2 \tag{2.90}$$

Now, we examine the ODE in radial direction (Eq. 2.15). For $\beta = 0$, Eq. 2.15 reduces to

$$R_0'' + \frac{1}{r} R_0' = 0 \tag{2.91}$$

The solution to Eq. 2.91 is

$$R_0(r) = a_3 \ln(r) + a_4 \tag{2.92}$$

Using the second boundary condition,

$$R_0(r_e) = a_3 \ln(r_e) + a_4 = 0 \quad \rightarrow \quad a_4 = -a_3 \ln(r_e) \tag{2.93}$$

Substituting the value of a_4 in Eq. 2.92, we get

$$R_0(r) = a_3 \ln(r) - a_3 \ln(r_e) = -a_3 \ln(\frac{r_e}{r}) = a_5 \ln(\frac{r_e}{r}) \tag{2.94}$$

The solution for $\beta = 0$ is

$$\Delta p_0(r,x) = R_0(r) X_0(x) = a_5 \ln(\frac{r_e}{r}) a_2 = F_0 \ln(\frac{r_e}{r}) \tag{2.95}$$

2.3.2 Case 2; $\beta = -\lambda^2 < 0$

For $\beta = -\lambda^2 < 0$, all the results expressed in Eqs. 2.26, 2.27 and 2.28 apply. Therefore, we have

$$X(x) = a_3 \cosh\left(\lambda \sqrt{k_r / k_x}\, x\right) \tag{2.96}$$

$$X'(x) = a_3\, \lambda \sqrt{k_r / k_x} \sinh\left(\lambda \sqrt{k_r / k_x}\, x\right) \tag{2.97}$$

Using the third boundary condition prevailing in semi-radial configuration (Eq.2.86)

$$X'(L_c) = a_3\, \lambda \sqrt{k_r / k_x} \sinh\left(\lambda \sqrt{k_r / k_x}\, L_c\right) = 0 \tag{2.98}$$

For Eq. 2.98 to hold, either $a_3 = 0$ or $\sinh\left(\lambda \sqrt{k_r / k_x}\, L_c\right) = 0$. The term $\sinh\left(\lambda \sqrt{k_r / k_x}\, L_c\right)$ can not be zero unless $\lambda = 0$. Therefore, $a_3 = 0$ and consequently $X(x) = 0$. $\beta = -\lambda^2 < 0$ yields a trivial solution.

2.3.3 Case 3; $\beta = \lambda^2 > 0$

For $\beta = \lambda^2 > 0$, all the results reported in Eqs. 2.30, 2.31, 2.32 and 2.33 hold. Hence, we have

$$X(x) = a_5 \cos\left(\lambda \sqrt{k_r / k_x}\, x\right) \tag{2.99}$$

Taking the derivative of Eq. 2.99 respect to x,

$$X'(x) = -a_5\, \lambda \sqrt{k_r / k_x} \sin\left(\lambda \sqrt{k_r / k_x}\, x\right) \tag{2.100}$$

Using the third boundary condition ($X'(L_c) = 0$),

$$X'(L_c) = -a_5 \lambda\sqrt{k_r/k_x}\sin\left(\lambda\sqrt{k_r/k_x}\,L_c\right) = 0 \tag{2.101}$$

For Eq. 2.101 to hold, either $a_5 = 0$ or $\sin\left(\lambda\sqrt{k_r/k_x}\,L_c\right) = 0$. Between these two cases, the choice of $a_5 = 0$ leads to a trivial solution. Hence, we consider the second case of $\sin\left(\lambda\sqrt{k_r/k_x}\,L_c\right) = 0$. The expression $\sin\left(\lambda\sqrt{k_r/k_x}\,L_c\right) = 0$ requires that $\lambda\sqrt{k_r/k_x}\,L_c = n\pi$ where n=1,2,3,.... Hence, the eigenvalues are determined to be

$$\lambda_n = \frac{n\pi}{L_c\sqrt{k_r/k_x}} \qquad \text{n=1,2,3,.....} \tag{2.102}$$

The eigenfunctions are

$$X_n(x) = a_5\cos\left(\lambda_n\sqrt{k_r/k_x}\,x\right) = a_5\cos\left(\frac{n\pi x}{L_c}\right) \tag{2.103}$$

For $\beta = \lambda^2 > 0$, the results in Eqs. 2.38 and 2.39 are valid.

$$R_n(r) = A_n I_0(\lambda_n r) + B_n K_0(\lambda_n r) \tag{2.38}$$

Applying the second boundary condition on Eq. 2.84, we have

$$R(r_e) = A_n I_0(\lambda_n r_e) + B_n K_0(\lambda_n r_e) = 0 \quad \rightarrow \quad B_n = -A_n\frac{I_0(\lambda_n r_e)}{K_0(\lambda_n r_e)} \tag{2.104}$$

Inserting Eq. 2.104 into Eq. 2.38,

$$R_n(r) = A_n I_0(\lambda_n r) - A_n \frac{I_0(\lambda_n r_e)}{K_0(\lambda_n r_e)} K_0(\lambda_n r) = A_n I_0(\lambda_n r_e)\left[\frac{I_0(\lambda_n r)}{I_0(\lambda_n r_e)} - \frac{K_0(\lambda_n r)}{K_0(\lambda_n r_e)}\right] \tag{2.105}$$

Multiplying the solutions for $X_n(x)$ and $R_n(r)$, we obtain

$$\begin{aligned}\Delta p_n(r,x) &= C_n I_0(\lambda_n r_e)\left[\frac{I_0(\lambda_n r)}{I_0(\lambda_n r_e)} - \frac{K_0(\lambda_n r)}{K_0(\lambda_n r_e)}\right] A_n \cos\left(\frac{n\pi x}{L_c}\right) \\ &= F_n I_0(\lambda_n r_e)\left[\frac{I_0(\lambda_n r)}{I_0(\lambda_n r_e)} - \frac{K_0(\lambda_n r)}{K_0(\lambda_n r_e)}\right] \cos\left(\frac{n\pi x}{L_c}\right)\end{aligned} \tag{2.106}$$

The complete solution is obtained by superposing all the individual solutions.

$$\Delta p(r,x) = \Delta p_0(r,x) + \sum_{n=1}^{\infty} \Delta p_n(r,x) \tag{2.107}$$

$$\Delta p(r,x) = F_0 \ln\left(\frac{r_e}{r}\right) + \sum_{n=1}^{\infty} F_n I_0(\lambda_n r_e)\left[\frac{I_0(\lambda_n r)}{I_0(\lambda_n r_e)} - \frac{K_0(\lambda_n r)}{K_0(\lambda_n r_e)}\right] \cos\left(\frac{n\pi x}{L_c}\right) \tag{2.108}$$

Taking the derivative of Eq. 108 with respect to r variable,

$$\frac{\partial(\Delta p)}{\partial r} = -\frac{1}{r} F_0 + \sum_{n=1}^{\infty} F_n \lambda_n I_0(\lambda_n r_e)\left[\frac{I_1(\lambda_n r)}{I_0(\lambda_n r_e)} + \frac{K_1(\lambda_n r)}{K_0(\lambda_n r_e)}\right] \cos\left(\frac{n\pi x}{L_c}\right) \tag{2.109}$$

To determine the coefficients F_0 and F_n, we use the first boundary condition.

$$r_p \left.\frac{\partial(\Delta p)}{\partial r}\right|_{r_p} = -F_0 + \sum_{n=1}^{\infty} F_n \lambda_n r_p I_0(\lambda_n r_e)\Omega_{rn}(r_p)\cos\left(\frac{n\pi x}{L_c}\right) = G(x) \tag{2.110}$$

where,

$$\Omega_{rn}(r_p) = \frac{I_1(\lambda_n r_p)}{I_0(\lambda_n r_e)} + \frac{K_1(\lambda_n r_p)}{K_0(\lambda_n r_e)} \tag{2.111}$$

The expression in Eq. 2.110 is a regular Fourier series expansion of the function $G(x)$.

$$\begin{aligned}
-F_0 &= \frac{1}{L_c}\int_0^{L_c} G(x)\,dx \\
&= \frac{1}{L_c}\frac{-\mu}{2\pi\alpha k_r}\sum_{i=1}^{N}\int_0^{L_c}\frac{q_i}{\Delta L_{pi}}\left\{H\left[x-(i-1)\Delta L_{pi}\right]-H\left[x-i\Delta L_{pi}\right]\right\}dx \\
&= \frac{1}{L_c}\frac{-\mu}{2\pi\alpha k_r}\sum_{i=1}^{N}\int_{(i-1)\Delta L_{pi}}^{i\Delta L_{pi}}\frac{q_i}{\Delta L_{pi}}dx = \frac{1}{L_c}\frac{-\mu}{2\pi\alpha k_r}\sum_{i=1}^{N}\frac{q_i}{\Delta L_{pi}}x\Big|_{(i-1)\Delta L_{pi}}^{i\Delta L_{pi}} \\
&= \frac{1}{L_c}\frac{-\mu}{2\pi\alpha k_r}\sum_{i=1}^{N}\frac{q_i}{\Delta L_{pi}}\Delta L_{pi} = \frac{1}{L_c}\frac{-\mu}{2\pi\alpha k_r}\sum_{i=1}^{N} q_i = \frac{-q_t}{2\pi\alpha k_r L_c}
\end{aligned} \tag{2.112}$$

After evaluating all integrals, the final expression for F_0 is

$$F_0 = \frac{\mu q_t}{2\pi\alpha\, k_r L_c} \tag{2.113}$$

The coefficient F_n could be determined as below.

$$F_n \lambda_n r_p I_0(\lambda_n r_e)\Omega_{rn}(r_p) = \frac{2}{L_c}\int_0^{L_c} G(x)\cos\left(\frac{n\pi x}{L_c}\right)dx \tag{2.114}$$

The integral at the right-hand-side of Eq. 2.114 is evaluated as bellow.

$$\int_0^{L_c} G(x)\cos\left(\frac{n\pi x}{L_c}\right)dx =$$

$$= \frac{-\mu}{2\pi\alpha k_r}\sum_{i=1}^{N}\int_0^{L_c}\frac{q_i}{\Delta L_{pi}}\left\{H\left[x-(i-1)\Delta L_{pi}\right]-H\left[x-i\Delta L_{pi}\right]\right\}\cos\left(\frac{n\pi x}{L_c}\right)dx$$

$$= \frac{-\mu}{2\pi\alpha k_r}\sum_{i=1}^{N}\frac{q_i}{\Delta L_{pi}}\int_{(i-1)\Delta L_{pi}}^{i\Delta L_{pi}}\cos(n\pi x/L_c)\,dx$$

$$= \frac{-\mu}{2\pi\alpha k_r}\sum_{i=1}^{N}\frac{q_i}{\Delta L_{pi}}\frac{L_c}{n\pi}\sin(n\pi x/L_c)\Big|_{(i-1)\Delta L_{pi}}^{i\Delta L_{pi}}$$

$$= \frac{-\mu}{2\pi\alpha k_r}\frac{L_c}{\pi}\sum_{i=1}^{N}\frac{q_i}{\Delta L_{pi}}\frac{1}{n}R_{rni} \tag{2.115}$$

where

$$R_{rni} = \sin\left[\frac{n\pi i\Delta L_{pi}}{L_c}\right]-\sin\left[\frac{n\pi(i-1)\Delta L_{pi}}{L_c}\right] \tag{2.116}$$

Substituting Eq. 2.115 into Eq. 2.114,

$$F_n \lambda_n r_p I_0(\lambda_n r_e)\,\Omega_{rn}(r_p) = \frac{2}{L_c}\frac{-\mu}{2\pi\alpha k_r}\frac{L_c}{\pi}\sum_{i=1}^{N}\frac{q_i}{\Delta L_{pi}}\frac{1}{n}R_{rni} \tag{2.117}$$

Rearranging for F_n,

$$F_n = \frac{-\mu}{2\pi\alpha\, k_r}\frac{2}{\pi r_p}\sum_{i=1}^{N}\frac{q_i}{\Delta L_{pi}}\frac{1}{n}\frac{R_{rni}}{\lambda_n I_0(\lambda_n r_e)\,\Omega_{rn}(r_p)} \tag{2.118}$$

Substituting Eqs.2.113 and 2.118 into Eq.2.109, we obtain

$$\Delta p(r,x) = \frac{q_t\mu}{2\pi\alpha\, k_r L_c}\ln\left(\frac{r_e}{r}\right) - \frac{\mu}{2\pi\alpha\, k_r}\frac{2}{\pi r_p}\sum_{i=1}^{N}\frac{q_i}{\Delta L_{pi}}\sum_{n=1}^{\infty}\frac{\psi_{rn}(r)R_{rni}\cos(n\pi x/L_c)}{n\lambda_n} \tag{2.119}$$

where,

$$\psi_{rn}(r) = \frac{\dfrac{I_0(\lambda_n r)}{I_0(\lambda_n r_e)} - \dfrac{K_0(\lambda_n r)}{K_0(\lambda_n r_e)}}{\dfrac{I_1(\lambda_n r_p)}{I_0(\lambda_n r_e)} + \dfrac{K_1(\lambda_n r_p)}{K_0(\lambda_n r_e)}} \tag{2.120}$$

Evaluating the solution given in Eq. 2.120 at the sandface of the jth perforation segment,

$$\Delta p_{pj}(r_{pj},x) = \frac{q_t\mu}{2\pi\alpha\, k_r L_c}\ln\left(\frac{r_e}{r_{pj}}\right) - \frac{\mu}{2\pi\alpha k}\frac{2}{\pi r_p}\sum_{i=1}^{N}\frac{q_i}{\Delta L_{pi}}\sum_{n=1}^{\infty}\psi_{rnj}(r_{pj})R_{rni}\cos(n\pi x/L_c) \tag{2.121}$$

$$\psi_{rnj}(r_{pj}) = \frac{\dfrac{I_0(\lambda_n r_{pj})}{I_0(\lambda_n r_e)} - \dfrac{K_0(\lambda_n r_{pj})}{K_0(\lambda_n r_e)}}{\dfrac{I_1(\lambda_n r_p)}{I_0(\lambda_n r_e)} + \dfrac{K_1(\lambda_n r_p)}{K_0(\lambda_n r_e)}} \tag{2.122}$$

Applying the pressure averaging method,

$$\Delta\tilde{p}_{pj} = \frac{1}{\Delta L_{pj}} \frac{q_t \mu}{2\pi \alpha\, k_r\, L_c} \ln\left(\frac{r_e}{r_{pj}}\right) \int_{j-1)\Delta L_{pi}}^{j\,\Delta L_{pi}} dx - \frac{\mu}{2\pi\alpha\, k_r} \frac{2}{r_p\, \pi} \sum_{i=1}^{N} \frac{q_i}{\Delta L_{pi}\, \Delta L_{pj}} \sum_{n=1}^{\infty} \frac{\psi_{rnj}(r_{pj})}{n\lambda_n} R_{rni}$$
$$\times \int_{(j-1)\Delta L_{Pj}}^{j\Delta L_{Pj}} \cos\left(\frac{n\pi x}{L_c}\right) dx \qquad (2.123)$$

Evaluating the integral on the right-hand-side of the Eq. 2.123,

$$\int_{j-1)\Delta L_{pj}}^{j\,\Delta L_{pj}} \cos(n\pi x/L_c) dx = \frac{L_c}{n\pi} \sin(n\pi x/L_c) \Big|_{(j-1)\Delta L_{pj}}^{j\,\Delta L_{pj}} = \frac{L_c}{n\pi} R_{rnj} \qquad (2.124)$$

Substituting Eq. 2.124 into Eq. 2.123

$$\Delta\tilde{p}_{pj} = \frac{q_t \mu}{2\pi\alpha\, k_r\, L_c} \ln\left(\frac{r_e}{r_{pj}}\right) - \frac{\mu}{2\pi\alpha\, k_r} \frac{2L_c}{r_p\, \pi^2} \frac{1}{\Delta L_{pj}} \sum_{i=1}^{N} \frac{q_i}{\Delta L_{pi}} \sum_{n=1}^{\infty} \frac{\psi_{rnj}(r_{pj})}{n^2 \lambda_n} R_{rni}\, R_{rnj} \qquad (2.125)$$

Inserting the expression for eigenvalue, $\lambda_n = n\pi / L_c \sqrt{k_r / k_x}$, into Eq. 2.125, we obtain

$$\Delta\tilde{p}_{pj} = \frac{q_t \mu}{2\pi\alpha\, k_r\, L_c} \ln\left(\frac{r_e}{r_{pj}}\right) - \frac{\mu}{2\alpha\, \pi \sqrt{k_r\, k_x}} \frac{2L_c^{\,2}}{\pi^3 r_p} \sum_{i=1}^{N} \frac{q_i}{\Delta L_{pi}\, \Delta L_{pj}} \sum_{n=1}^{\infty} \frac{\psi_{rnj}(r_{pj}) R_{rni}\, R_{rnj}}{n^3} \qquad (2.126)$$

Now, we add the skin factor.

$$\Delta\tilde{p}_{tj} = \frac{q_t \mu}{2\pi\alpha k_r L_c}\ln\left(\frac{r_e}{r_{pj}}\right) - \frac{\mu}{2\alpha\pi\sqrt{k_r k_x}}\frac{2L_c^{\,2}}{\pi^3 r_p}\sum_{i=1}^{N}\frac{q_i}{\Delta L_{pi}\Delta L_{pj}}\sum_{n=1}^{\infty}\frac{\psi_{rnj}(r_{pj})R_{rni}R_{rnj}}{n^3}$$

$$+\frac{q_j \mu}{2\pi\alpha k_r \Delta L_{pj}} s_{czj} \tag{2.127}$$

Defining

$$B_{j0} = \frac{\mu}{2\pi\alpha k_r L_c}\ln\left(\frac{r_e}{r_{pj}}\right) \tag{2.128}$$

$$B_{ji} = -\frac{\mu}{2\pi\alpha\sqrt{k_r k_x}}\frac{2L_c^{\,2}}{\pi^3 r_p}\frac{1}{\Delta L_{pi}\Delta L_{pj}}\sum_{n=1}^{\infty}\frac{1}{n^3}\psi_{rnj}(r_{pj})R_{rni}R_{rnj} \tag{2.129}$$

$$B_{jj} = -\frac{\mu}{2\pi\alpha\sqrt{k_r k_x}}\frac{2L_c^{\,2}}{\pi^3 r_p}\frac{1}{\Delta L_{pi}\Delta L_{pj}}\sum_{n=1}^{\infty}\frac{\psi_{rnj}(r_{pj})R_{rni}R_{rnj}}{n^3} + \frac{\mu}{2\pi\alpha\Delta L_{pj}k_r}s_{czj} \tag{2.130}$$

The final solution may be expresses as below.

$$\Delta p_{tj} = B_{j0}q_t + \sum_{i=1}^{N} q_i B_{ji} \tag{2.131}$$

Imposing the infinite-conductivity condition and writing Eq. 2.131 for all segments, we obtain

$$\text{j=1} \qquad \Delta p_{t1} = B_{10} q_t + \sum_{i=1}^{N} q_i B_{1i} = \Delta p_{tm} \tag{2.132}$$

$$\text{j=2} \qquad \Delta p_{t2} = B_{20} q_t + \sum_{i=1}^{N} q_i B_{2i} = \Delta p_{tm} \tag{2.133}$$

$$\text{j=3} \qquad \Delta p_{t3} = B_{30} q_t + \sum_{i=1}^{N} q_i B_{3i} = \Delta p_{tm} \tag{2.134}$$

$$\text{j=N-1} \qquad \Delta p_{t(N-1)} = B_{(N-1)0} q_t + \sum_{i=1}^{N} q_i B_{(N-1)i} = \Delta p_{tm} \tag{2.135}$$

$$\text{j=N} \qquad \Delta p_{tN} = B_{N0} q_t + \sum_{i=1}^{N} q_i B_{Ni} = \Delta p_{tm} \tag{2.136}$$

Recasting Eqs. 2.79 and 2.132 through 2.136 into a matrix format,

$$\begin{bmatrix} 1 & -1 & -1 & -1 & \ldots & -1 \\ B_{10} & B_{11} & B_{12} & B_{13} & \ldots & B_{1N} \\ B_{20} & B_{21} & B_{22} & B_{23} & \ldots & B_{2N} \\ \cdot & \cdot & \cdot & \cdot & & \cdot \\ \cdot & \cdot & \cdot & \cdot & & \cdot \\ \cdot & \cdot & \cdot & \cdot & & \cdot \\ \cdot & \cdot & \cdot & \cdot & & \cdot \\ B_{N0} & B_{N1} & B_{N2} & B_{N3} & & B_{NN} \end{bmatrix} \begin{bmatrix} q_t \\ q_1 \\ q_2 \\ \cdot \\ \cdot \\ \cdot \\ \cdot \\ q_N \end{bmatrix} = \begin{bmatrix} 0 \\ \Delta p_{tm} \\ \Delta p_{tm} \\ \cdot \\ \cdot \\ \cdot \\ \cdot \\ \Delta p_{tm} \end{bmatrix} \tag{2.137}$$

2.4 Model for Radial-Axial Laboratory Flow Target

In the radial-axial laboratory flow configuration, fluid is simultaneously injected at the cylindrical surface and the un-perforated surface of the core during the test. Fig. 2.3 is a schematic of the boundary conditions in radial-axial laboratory flow target.

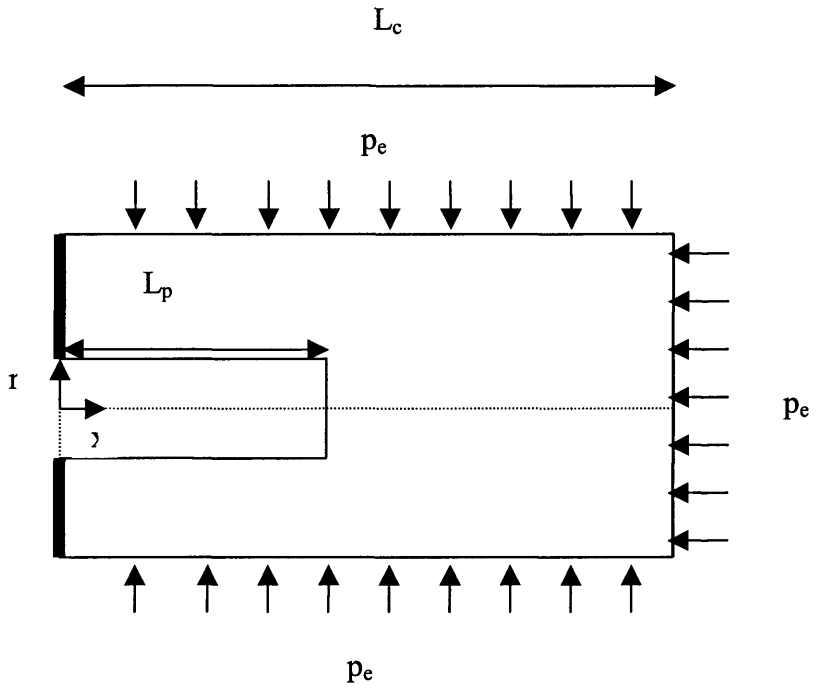

Figure 2.4 - A schematic of radial-axial laboratory flow target.

Eq. 2.1 describes the physics of the single-phase flow across the perforated core targets with radial-axial geometry. The first and fourth boundary conditions presented in

Eq. 2.3 and 2.6 also pertain to the radial-axial configuration. The second boundary condition is the same for both, the radial-axial and semi-radial flow configurations. The third boundary condition for the radial-axial arrangement is the same as that for the axial design. The second and third boundary conditions for the radial-axial geometry are

$$2.\ \Delta p(r_e, x) = 0 \tag{2.82}$$

$$3.\ \Delta p(r, L_c) = 0 \tag{2.5}$$

As before, we use the separation of variables method to find the solution for radial-axial case. The ordinary differential equations presented in Eqs. 2.15 and 2.16 apply. The application of separation of variables to the fourth boundary condition leads to $X'(0)$, which is the same as the two previous cases considered. Separation of variables applied to the second and third boundary conditions results in Eqs. 2.85 and 2.18

$$2.\quad R(r_e) = 0 \tag{2.85}$$

$$4.\quad X(L_c) = 0 \tag{2.18}$$

Now, we solve Eqs. 2.15 and 2.16 under the boundary conditions specified in Eqs. 2.3, 2.85, 2.18 and 2.6.

2.4.1 Case 1; $\beta = 0$

For $\beta = 0$, the solution to Eq. 2.16 is as given in Eqs. 2.20, 2.21 and 2.22. As shown in Eqs. 2.23 and 2.24, $\beta = 0$ results in a trivial solution.

2.4.2 Case 2; $\beta = -\lambda^2 < 0$

For $\beta = -\lambda^2 < 0$ case, the ODE in x direction and its solution are as given in Eqs. 2.25, 2.26 and 2.27. Imposing the boundary conditions presented in Eqs. 2.18 and 2.6 on the solutions expressed in Eqs. 2.26 and 2.27, we obtain a trivial solution as illustrated in Eqs. 2.27 and 2.28.

2.4.3 Case 3; $\beta = \lambda^2 > 0$

For $\beta = \lambda^2 > 0$, the solution to Eq. 2.16 is presented in Eqs. 2.30 through 2.35 in section 2.2.3. The final solution is

$$\lambda_n = \frac{(2n-1)\pi}{2L_c}\sqrt{k_x/k_r} \tag{2.35}$$

$$X_n(x) = a_n \cos\left[\frac{(2n-1)\,\pi\, x}{2\,L_c}\right] \tag{2.36}$$

For $\beta = \lambda^2 > 0$, the solution to Eq. 2.15 is as described in Eqs. 2.38, 2.104 and 2.105.

$$R_n(r) = C_n I_0(\lambda_n r_e)\left[\frac{I_0(\lambda_n r)}{I_0(\lambda_n r_e)} - \frac{K_0(\lambda_n r)}{K_0(\lambda_n r_e)}\right] \tag{2.105}$$

Multiplying Eqs. 2.36 and 2.105 and applying the superposition principle, we obtain the pressure drop solution.

$$\Delta p(r,x)=\sum_{n=1}^{\infty}F_n I_0(\lambda_n r_e)\left[\frac{I_0(\lambda_n r)}{I_0(\lambda_n r_e)}-\frac{K_0(\lambda_n r)}{K_0(\lambda_n r_e)}\right]\cos\left[\frac{(2n-1)\,\pi\, x}{2\,L_c}\right] \tag{2.138}$$

Taking the derivative of Eq. 2.138 with respect to r, we obtain

$$\frac{\partial(\Delta p)}{\partial r}=\sum_{n=1}^{\infty}F_n \lambda_n I_0(\lambda_n r_e)\left[\frac{I_1(\lambda_n r)}{I_0(\lambda_n r_e)}+\frac{K_1(\lambda_n r)}{K_0(\lambda_n r_e)}\right]\cos\left[\frac{(2n-1)\,\pi\, x}{2\,L_c}\right] \tag{2.139}$$

To find out the coefficients F_n, we use the first boundary condition.

$$r_p\frac{\partial(\Delta p)}{\partial r}\Big|_{r_p}=\sum_{n=1}^{\infty}F_n \lambda_n r_p I_0(\lambda_n r_e)\Omega_{rn}(r_p)\cos\left[\frac{(2n-1)\,\pi\, x}{2\,L_c}\right]=G(x) \tag{2.140}$$

A comparison of Eqs. 2.47 and 2.140 reveals that these two equations are nearly identical. The only exception is that the term $I_1(\lambda_n r_e)\,\Omega_{an}(r_p)$ in Eq. 2.47 is replaced by the term $I_0(\lambda_n r_e)\,\Omega_{rn}(r_p)$ in Eq. 2.140. Therefore, the coefficient F_n may be found by multiplying Eq. 2.140 by $\cos\left[\frac{(2m-1)\pi x}{2L_c}\right]$ and integrating the resulting expression in the interval $0\le x\le L_c$. The detail of the procedure is given in Eqs. 2.48 through 2.58. The final expression for the coefficient F_n is

$$F_n=-\frac{8\,\mu\, L_c}{2\pi\,\alpha\, r_p\sqrt{k_r k_x}}\frac{1}{\pi^2}\sum_{i=1}^{N}\frac{q_i}{\Delta L_{pi}}\frac{R_{ani}}{(2n-1)^2\Omega_{rn}(r_p)} \tag{2.141}$$

Substituting Eq. 2.141 into Eq. 2.138, we find the pressure solution.

$$\Delta p(r,x) = \frac{8\mu L_c}{2\pi\alpha r_p\sqrt{k_r k_x}}\frac{1}{\pi^2}\sum_{i=1}^{N}\frac{q_i}{\Delta L_{pi}}\sum_{n=1}^{\infty}\frac{\psi_{rn}(r)R_{ani}}{(2n-1)^2}\cos\left[\frac{(2n-1)\pi x}{2L_c}\right] \tag{2.142}$$

where the function $\psi_{rn}(r)$ is as given in Eq. 2.120. Evaluating the solution in Eq. 2.142 at the jth perforation segment,

$$\Delta p_{pj}(r_{pj},x) = \frac{8L_c\mu}{2\pi^3\alpha\sqrt{k_r k_x}\,r_p}\sum_{i=1}^{N}\frac{q_i}{\Delta L_{pi}}\sum_{n=1}^{\infty}\frac{\psi_{rnj}(r_{pj})R_{ani}}{(2n-1)^2}\cos\left[\frac{(2n-1)\pi x}{2L_c}\right] \tag{2.143}$$

where $\psi_{rnj}(r_{pj})$ is given in Eq. 2.122.

Applying the pressure averaging method as shown in Eqs. 2.63 through 2.66,

$$\Delta\tilde{p}_{pj} = \frac{\mu}{2\pi\alpha r_p\sqrt{k_r k_x}}\frac{16L_c^{\,2}}{\pi^3}\sum_{i=1}^{n}\frac{q_i}{\Delta L_{pi}\Delta L_{pj}}\sum_{n=1}^{\infty}\frac{\psi_{rnj}(r_{pj})R_{ani}R_{anj}}{(2n-1)^3} \tag{2.144}$$

Adding the skin factor,

$$\Delta p_{tj} = \frac{\mu}{2\pi\alpha r_p\sqrt{k_r k_x}}\frac{16L_c^{\,2}}{\pi^3}\sum_{i=1}^{n}\frac{q_i}{\Delta L_{pi}\Delta L_{pj}}\sum_{n=1}^{\infty}\frac{\psi_{rnj}(r_{pj})R_{ani}R_{anj}}{(2n-1)^3} + \frac{\mu}{2\pi\alpha k_r\Delta L_{pj}}s_{czj} \tag{2.145}$$

Eq. 2.145 may be simplified as bellow

$$\Delta p_{tj} = \sum_{i=1}^{N} q_i B_{ji} \tag{2.146}$$

where,

$$B_{ji} = \frac{\mu}{2\pi\alpha r_p \sqrt{k_r k_x}} \frac{16 L_c^{\,2}}{\pi^3} \frac{1}{\Delta L_{pi}\, \Delta L_{pj}} \sum_{n=1}^{\infty} \frac{\psi_{rnj}(r_{pj}) R_{ani} R_{anj}}{(2n-1)^3} \tag{2.147}$$

$$B_{jj} = -\frac{\mu}{2\pi\alpha r_p \sqrt{k_r k_x}} \frac{16 L_c^{\,2}}{\pi^3} \frac{1}{\Delta L_{pi}\, \Delta L_{pj}} \sum_{n=1}^{\infty} \frac{\psi_{rnj}(r_{pj}) R_{ani} R_{anj}}{(2n-1)^3} + \frac{\mu}{2\pi\alpha\, \Delta L_{pj}\, k_r} s_{czj} \tag{2.148}$$

Applying infinite conductivity condition, rewriting Eq. 2.146 for all the segments and combining the pressure equations with the rate equation, we end up with the matrix presented bellow.

$$\begin{bmatrix} 1 & -1 & -1 & -1 & \dots & -1 \\ 0 & B_{11} & B_{12} & B_{13} & \dots & B_N \\ 0 & B_{21} & B_{22} & B_{23} & \dots & B_{2N} \\ \cdot & \cdot & \cdot & \cdot & & \cdot \\ \cdot & \cdot & \cdot & \cdot & & \cdot \\ \cdot & \cdot & \cdot & \cdot & & \cdot \\ \cdot & \cdot & \cdot & \cdot & & \cdot \\ 0 & B_{N1} & B_{N2} & B_{N3} & & B_{NN} \end{bmatrix} \begin{bmatrix} q_t \\ q_1 \\ q_2 \\ \cdot \\ \cdot \\ \cdot \\ \cdot \\ q_N \end{bmatrix} = \begin{bmatrix} 0 \\ \Delta p_{tm} \\ \Delta p_{tm} \\ \cdot \\ \cdot \\ \cdot \\ \cdot \\ \Delta p_{tm} \end{bmatrix} \tag{2.149}$$

Eq. 2.149 is equivalent to Eq. 2.80. The only difference is that the expressions for the matrix coefficients (B_{ji}) are slightly different.

CHAPTER 3

VERIFICATION OF THE ANALYTICAL FLOW MODELS

3.1 Introduction

The new analytical models to calculate the core flow efficiency of perforated core targets have been presented in the previous chapter. The analytical post-perforation flow models have been coded in a FORTRAN environment. The compute codes are appended. The computer codes developed for the analytical models are very fast. The typical CPU time is in the order of 1-2% of a second. Hence, the new analytical solutions are inexpensive to compute.

In this chapter, the new models are compared with the models existing in the literature. The new analytical solution for axial core configuration is compared with the results from numerical finite difference and finite elements models. The solution presented for radial-axial geometry is tested against the results from a finite element simulation study. The analytical model for semi-radial core setup is compared with the existing analytical models for partially penetrating wells.

3.2 Verification of Axial Model

To verify the analytical solution developed for the axial flow geometry, the model has been compared against the results presented by Behie and Settari[13], Dogulu[15], Tariq.[20] The models presented by Dogulu[15] and Behie and Settari[13] are based on finite difference

approach. The results presented by Tariq[20] were obtained from a commercial finite element simulator. The results from all the models are displayed in Fig. 3.1. The basic data set used in the comparison study is documented in Fig. 3.1 as well. Fig. 3.1 shows the relationship between the perforation length and ideal flow rate for an axial flow configuration. The results from all the models agree very well for short perforations. The methods calculate somewhat different results for longer perforations. However, the differences among the methods are reasonably small. The results from our model and Dogulu's model agree in 5%.

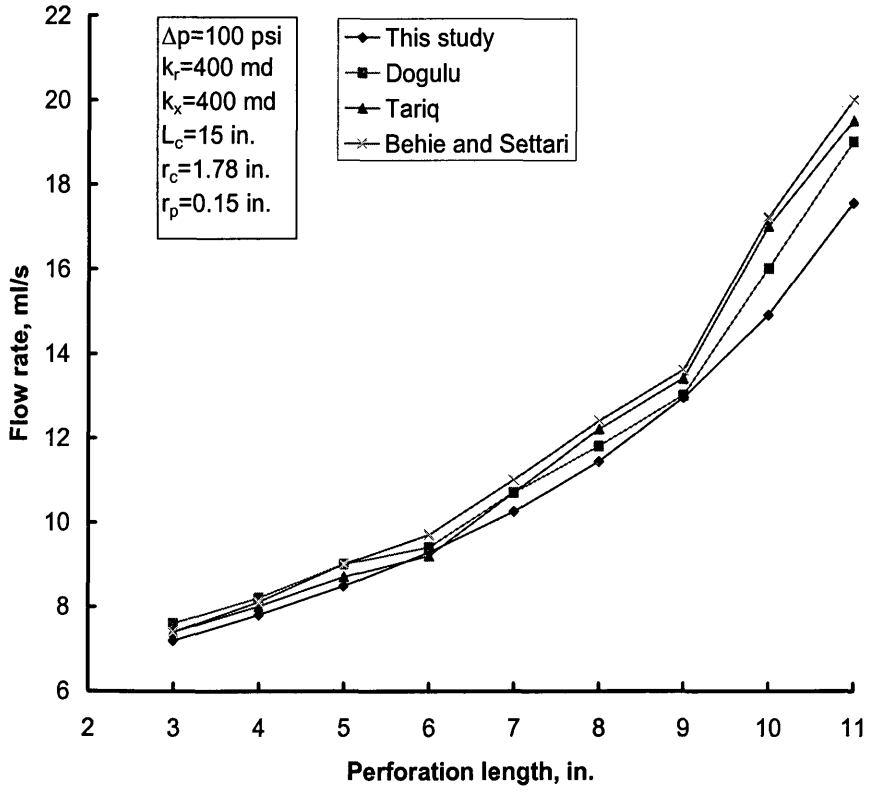

Figure 3.1 - Comparison of the axial model with the models in the literature.

The finite difference model developed by Dogulu could simulate the transient flow. To verify his model and the computer code, Dogulu compared his model against the analytical solution for a vertical well. In the comparison, the transient rate decline in a vertical well producing at a constant wellbore pressure is simulated. His comparison is presented in Fig. 3.2. He reported up to 9% error in the results from his finite difference model. The error in his model has stabilized around 5% at late times.

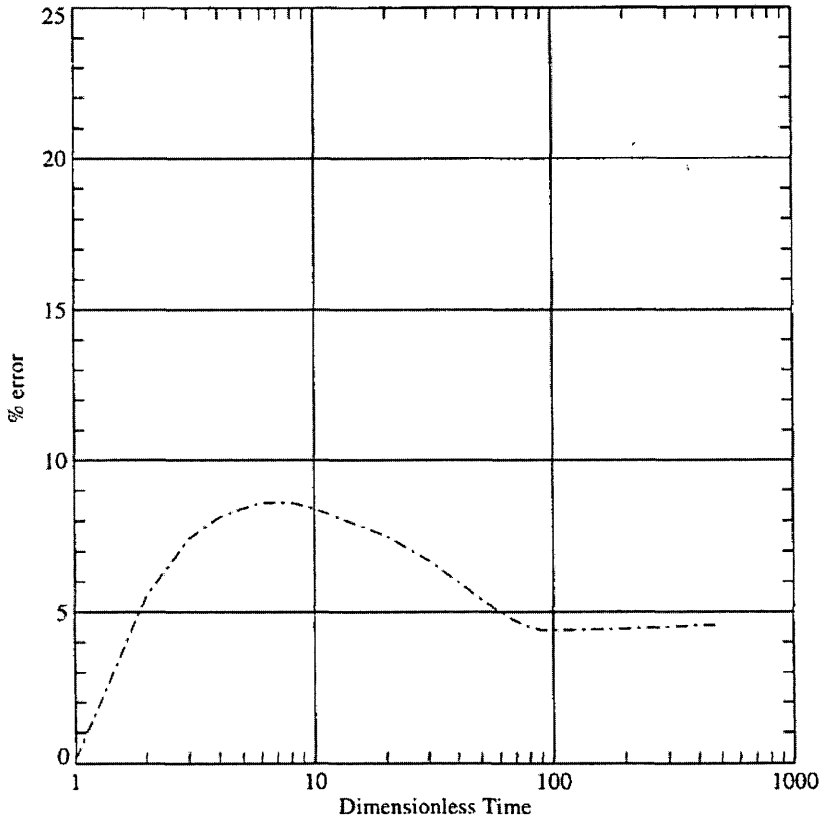

Figure 3.2 – Error analysis for Dogulu's finite difference model (Ref. 15).

3.3 Verification of Radial-Axial Model

To verify the new analytical solution for the radial-axial flow pattern, the solution has also been compared against the results presented by Deo et al.[8] They used a commercial finite element simulator (ANSYS) to generate their results. Fig. 3.3 displays the results from the new analytical solution and Deo et al.[8] model. The comparison is made in terms of the flux distribution along the perforation. Fig. 3.3 depicts the flux distribution along the perforation in the radial-axial laboratory flow target. The data set used in the comparison is reported on Fig. 3.3.

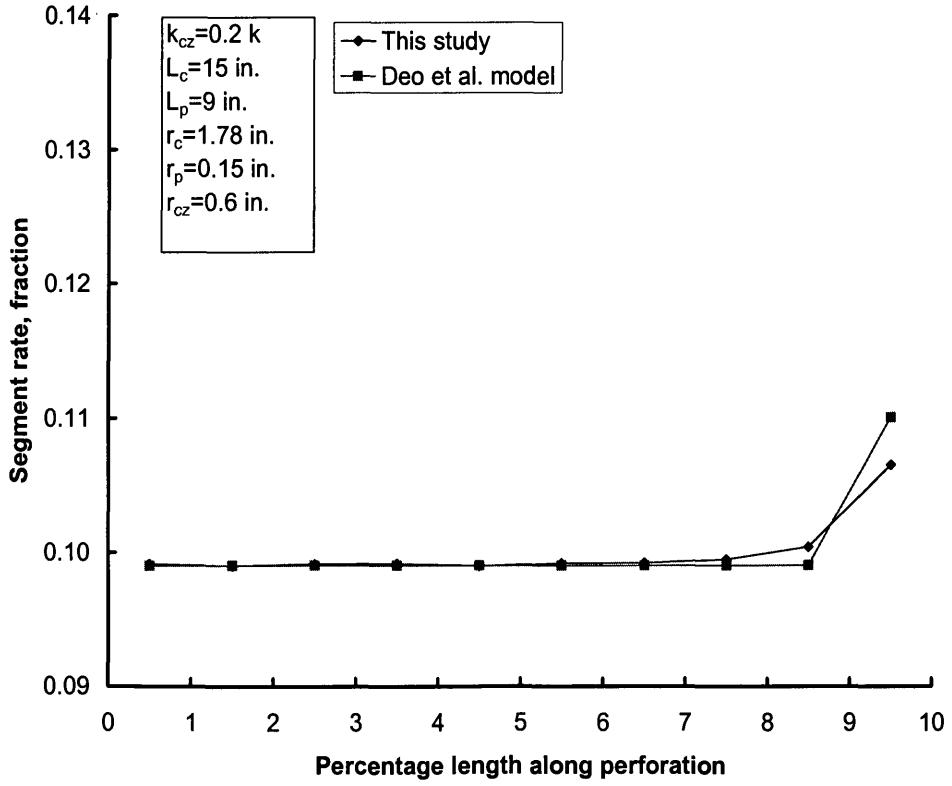

Figure 3.3 - Comparison of the radial-axial model with Deo et al.[8] model.

In general, the results from both models agree very well. However, our model indicates a somewhat different contribution from the last two segments than the Deo et al. model does.

3.4 Verification of Semi-Radial Model

The literature has not reported any results for the perforated core targets with semi-radial setup. The flow geometry in a perforated core with semi-radial configuration and that in a partially penetrating vertical well are equivalent. Therefore, the semi-radial flow model has been compared against the partially penetrating vertical well models existing in the literature. In the comparison, a partially penetrating well, with h=100 ft and r_w=0.25 ft, in an isotropic formation is considered. The comparison is made in terms of partial penetration pseudoskin as a function of the length of the completed interval which is located at the top of the formation. Fig. 3.4 shows the results from the semi-radial, Vrbik[25], and Yildiz and Cinar[26] models. An excellent agreement is observed among the models. It should be pointed out that the Vrbik and Yildiz and Cinar models for partially penetrating vertical wells consider a very large reservoir radius compared to wellbore radius. The aspect ratio of the core radius to the perforation radius on a perforated core target is not large enough. Hence, although Vrbik and Yildiz and Cinar models are accurate for partially penetrating wells, these models would not work for the post-perforation flow tests.

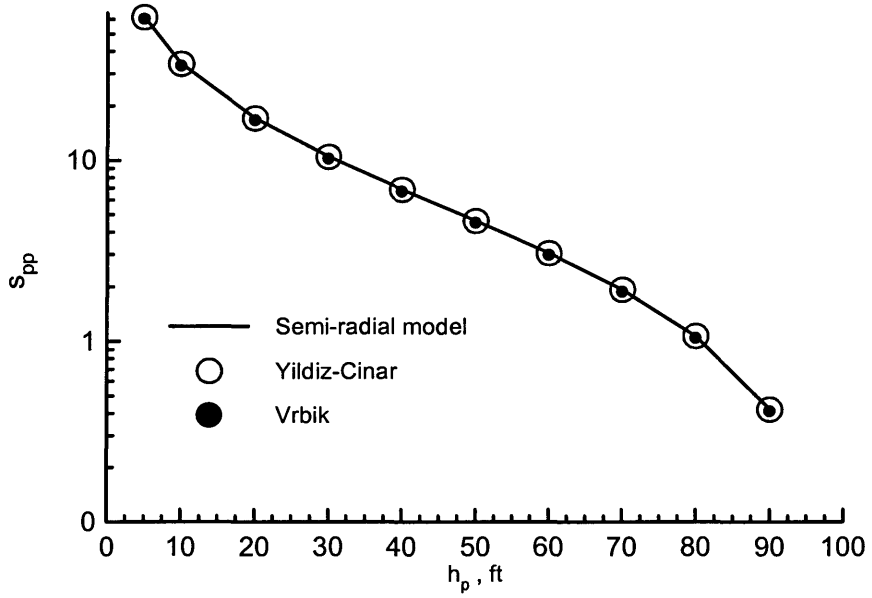

Figure 3.4 - Comparison of the semi-radial model with the existing models.

CHAPTER 4

APPLICATIONS AND DISCUSSION

4.1 Introduction

In this section, some unique applications of the flow models are presented. The impact of different perforation parameters on the flow efficiency of perforated core targets is investigated. A sensitivity study is conducted to identify the perforation parameters controlling the flow rate across the core, flux distribution, and core flow efficiency.

In all the simulated results presented in this section, the analytical flow models were run with the basic input data reported in Table 4.1. During the sensitivity study, some of the input data have been changed. The changes in the input data are documented either in text or on the figures.

The simulated results are sensitive to the number of segments representing the perforation. Sensitivity of the calculated results to the number of perforation segments has been investigated. It is observed that dividing a perforation into ten segments is enough to obtain accurate results.

Table 4.1- Basic input data

Δp, psi	50
μ, cp	0.7
k_r, md	200
k_x, md	200
L_c, in.	15
L_p, in.	10
r_c, in.	1.78
r_{cz}, in.	0.48
r_p, in.	0.15

4.2 Effect of Test Configuration on Flow Rate and Flux Distribution

Using the data set given in Table 4.1 and the computer codes developed for the axial, semi-radial, and radial-axial flow models, the effect of post-perforation flow test configuration on the total flow rate across the core and the flux distribution along the perforation are investigated.

Before we discuss the impact of flow configuration, it should be remembered that the flow configurations are directly related to the flow conditions at the external boundaries.

- In the axial flow, the fluid is only injected at the un-perforated end of the cylindrical core. The external cylindrical surface of the core is sealed.
- For the semi-radial configuration, the flow conditions at the external boundaries are the opposite of those for axial flow. The external cylindrical surface is exposed to fluid injection and the un-perforated end is sealed.

- In case of the radial-axial test setup, both the external cylindrical surface and un-perforated end of the core admit the injected fluid.

Fig. 4.1 displays the simulated flow rates as a function of the test configuration and the perforation length. It should be observed that the flow rates through a perforated core with the axial setup are much lower than those with the semi-radial and radial-axial configurations. As a matter of fact, the flow rates through the semi-radial and radial-axial configurations are about an order of magnitude higher than those through the axial test apparatus. Such a high difference in the computed flow rate is related to the external surface area open to flow and the degree of flow convergence around the perforation. The radial-axial and axial setups posses the largest and smallest external cross-sectional areas open to fluid flow, respectively. Additionally, the fluid experience more convergence and three dimensional flow effect in case of the axial flow geometry.

It should be also noticed that the flow rates computed for the semi-radial and radial-axial configurations are very close. The flow rates calculated for the radial-axial pattern is slightly higher than those for the semi-radial pattern. This is due to the fact that, in case of the radial-axial test geometry, the external surface area open to injected fluid is somewhat larger; this in turn lowers the velocity of the injected fluid. For all practical purposes, the flow rate responses to the radial-axial and semi-radial cases are nearly identical.

Fig. 4.1 shows that the flow rate increases almost linearly with the increase in perforation length as it should be expected. The reason for the increase in the flow rate is the fact that cross-sectional contact area between the perforation tunnel and the core target increases when the perforation is elongated. Larger contact area causes slower fluid velocity and lesser energy loss around the perforation tunnel.

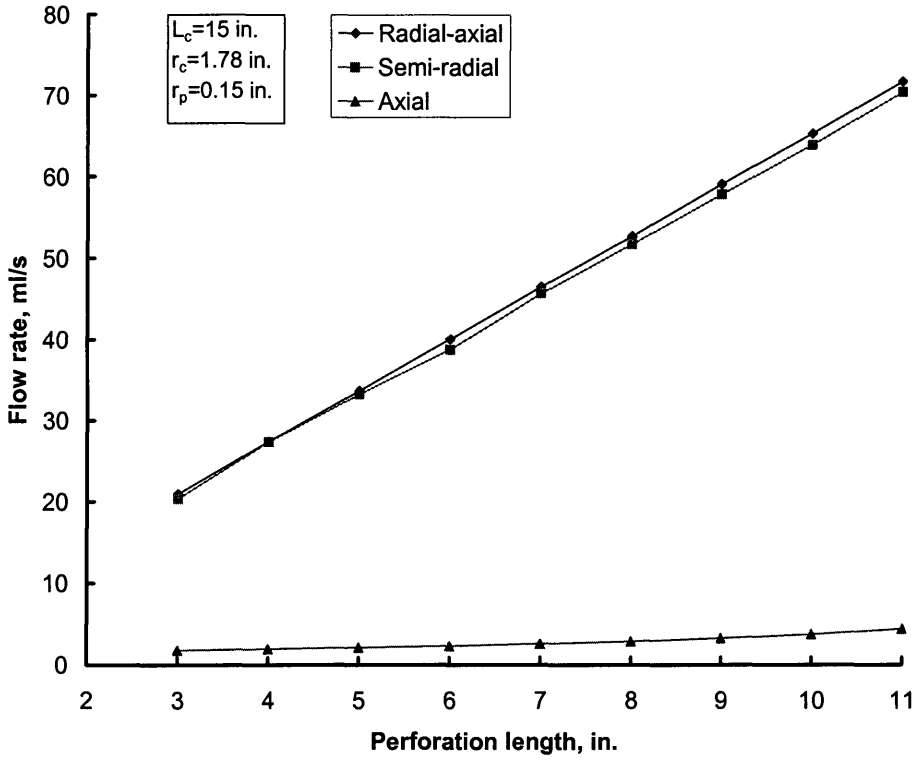

Figure 4.1 – Flow rate influenced by test configuration and perforation length.

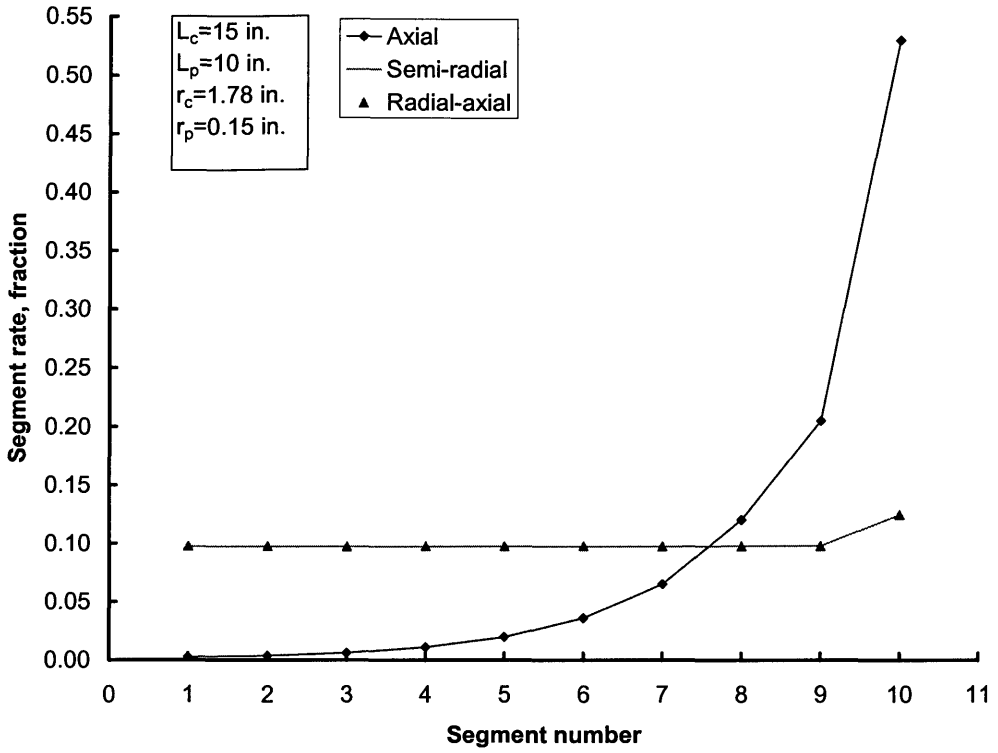

Figure 4.2 – Impact of test configuration on flux distribution along a 10-in. perforation.

The influence of flow test geometry on the flux distribution has been investigated on a 10-in long perforation. The flux distributions for all three flow configurations are displayed in Fig. 4.2. It should be noted that the semi-radial and radial-axial laboratory flow targets result in identical flux distributions. In these two configurations, the flux is almost uniformly distributed along the perforations. The only exception is that the last segment produces at a higher rate.

In the axial laboratory flow target, the segments closer to un-perforated end of the core, where the fluid is injected, produce at a significantly higher rate. The flux

distribution increases exponentially along the perforation. Any damage around the end of the perforation would severely decrease the efficiency of the perforation process.

4.3 Influence of Crushed Zone around Perforation Tunnel

In all the previous examples considered in the sensitivity studies and model verification section, we have considered an ideal perforation without any crushed zone around it. In actual practice, a thin zone of altered permeability and porosity is created around the perforation tunnel during the perforating operation. Shaped charge explosives fired during the perforating creates shock waves deforming the structure of the rock around the perforation tunnel. In many cases, the deformation due to shock waves generates a layer of rock with low permeability around the tunnel. In this text, the layer of rock with altered permeability and porosity around the perforation tunnel is referred to as the crushed zone. Based on the experimental studies, it is believed that the thickness of the crushed zone is in the order of ½ in. The permeability of the crushed zone may be as low as 5% of the original formation permeability. However, it is more common to have a reduced crushed zone permeability value in the order of 10-20% of the original permeability. Depending on the nature of the rock and operation conditions, in some rare cases, the shock waves may create small fractures around the perforation. In such cases, the permeability of the altered region around the perforation tunnel may actually be increased and a CFE greater than 1.0 may be encountered.

There is still an ongoing discussion on the nature of the altered zone around the perforation. Several research groups have measured the permeability profile along the perforation axis and it has been demonstrated that the altered permeability along the perforation is not constant. In a recent study, Halleck et al.[18] has measured an altered permeability profile varying almost linearly along the perforation tunnel.

Below, we consider different types of permeability damage around the perforation tunnel and investigate the impact of skin distribution around the perforation on the total flow rate, flux distribution, and core flow efficiency.

4.3.1 Uniform Skin Distribution

First, we investigate the impact of uniform skin distribution on the total flow rate across the perforated core target and the flux distribution along the core. A uniform skin factor of $s_{cz} = 4.6$ is considered for all three post-perforation flow configurations. The results are shown in Figs. 4.3 through 4.8.

Fig. 4.3 illustrates how the total flow rate across an axial target is affected by the skin factor. Two cases are considered; the first and second cases have a skin factor of 0 and 4.6, respectively. The results on Fig. 4.3 demonstrate that a skin factor of 4.6 reduces the total flow rate about 10-35%. When the perforation length increases, the impact of skin factor is pronounced more.

Figs. 4.4 and 4.5 depict the simulated results for the semi-radial and radial-axial core targets. Similar to previous case, a case with uniform skin factor of 4.6 is compared against the reference undamaged case. It can be observed that the semi-radial and radial-axial configurations are more vulnerable to skin factor than the axial setup. The same skin factor of $s_{cz} = 4.6$, yielding 10-35% reduction in the flow rate across the axial setup, results in 75-85% loss in the flow rates across the core targets with the semi-radial and radial- axial configurations. It can be also seen that the results for the semi-radial and radial-axial cases are almost identical.

The effect of the skin factor on the flux distribution along the perforation tunnel is also investigated. The results for the axial, semi-radial, and radial-axial cases are presented in Figs. 4.6, 4.7, and 4.8, respectively. For all three configurations, the flux

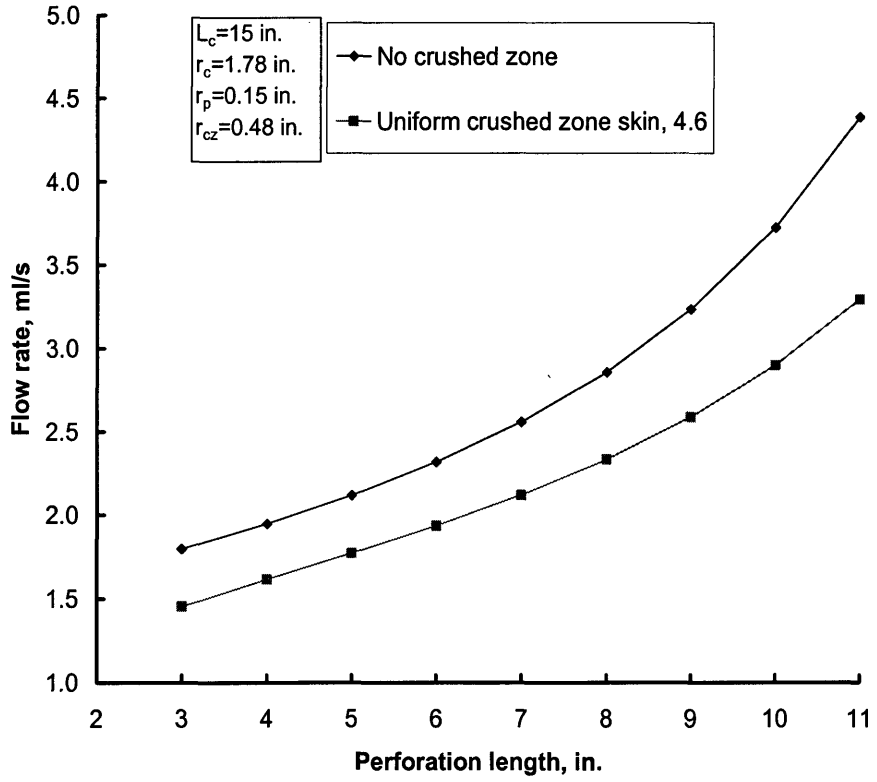

Figure 4.3 – Effect of uniform skin on the flow across an axial target.

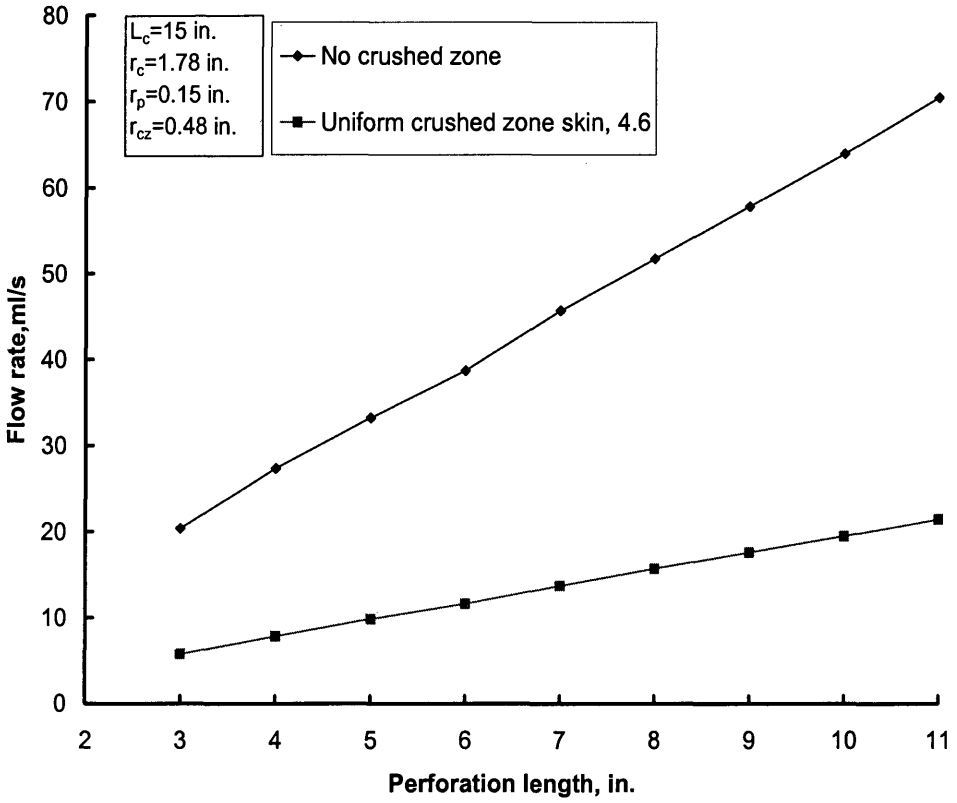

Figure 4.4 – Impact of uniform skin factor on flow rate - Semi-radial flow target.

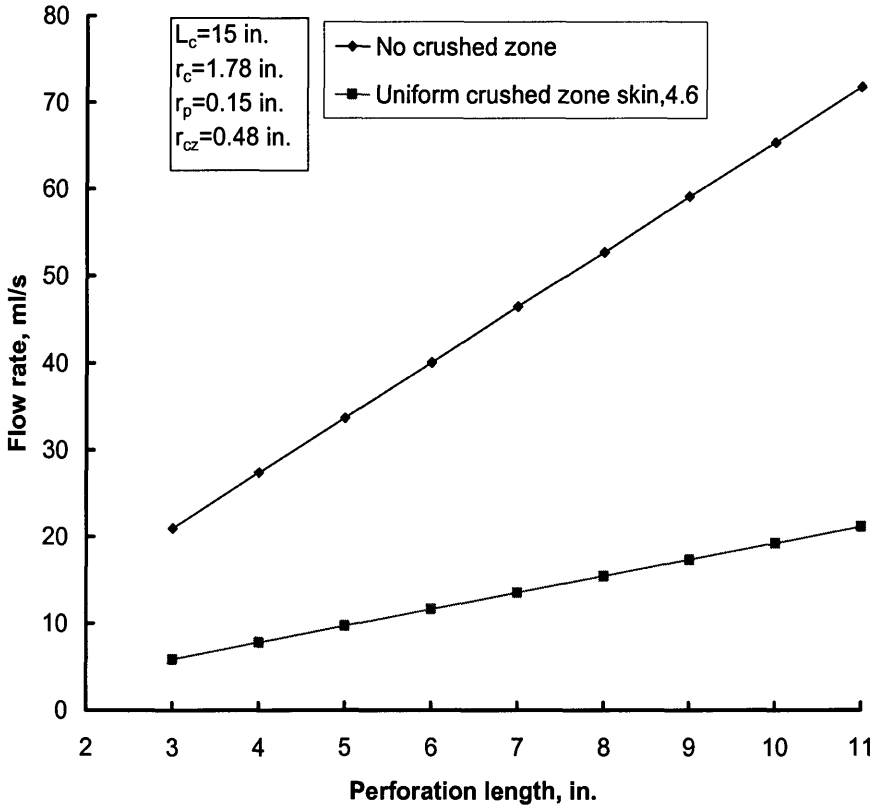

Figure 4.5 –Influence of uniform skin factor on flow rate – Radial-axial flow target.

distributions under undamaged and uniformly damaged conditions are compared.

Fig. 4.6 demonstrates how the flux distribution on an axial configuration varies with the skin factor. It should be noticed that, compared to the base case of undamaged perforation, a uniform skin factor of $s_{cz} = 4.6$ changes the flux distribution substantially. Uniform skin distribution increases the contribution of the segments closer to perforation entry and decreases the contribution of segments closer to the tip of the perforation.

Fig. 4.7 shows the effect of a uniform skin factor on the flux distribution along the perforation with a semi-radial flow configuration. A uniform skin factor of $s_{cz} = 4.6$ decreases the contribution of the last segment at the perforation tip and makes the flux distribution nearly uniform. Almost identical results may also be observed for the radial-axial geometry as shown in Fig. 4.8.

4.3.2 Non-Uniform Skin Distribution

In the previous section, we compared the uniform skin distribution case against the base case of undamaged perforation. The uniform skin distribution assumption is not realistic. Based on the experimental studies and theoretical considerations, it has been concluded that the fluidized jet creating the perforation has a higher velocity and power at the perforation entry. Its velocity decreases along the perforation trajectory. Hence, the rock destruction is much more severe at the perforation entrance. The destructive power of the fluidized jet decreases along the perforation tunnel. Additionally, due to heterogeneous nature of the rock itself, the rock may show locally differing resistance to jet power.

In general, the damage around the perforation tunnel is not uniform and it varies along the perforation axis as reported in the literature.[14, 18]

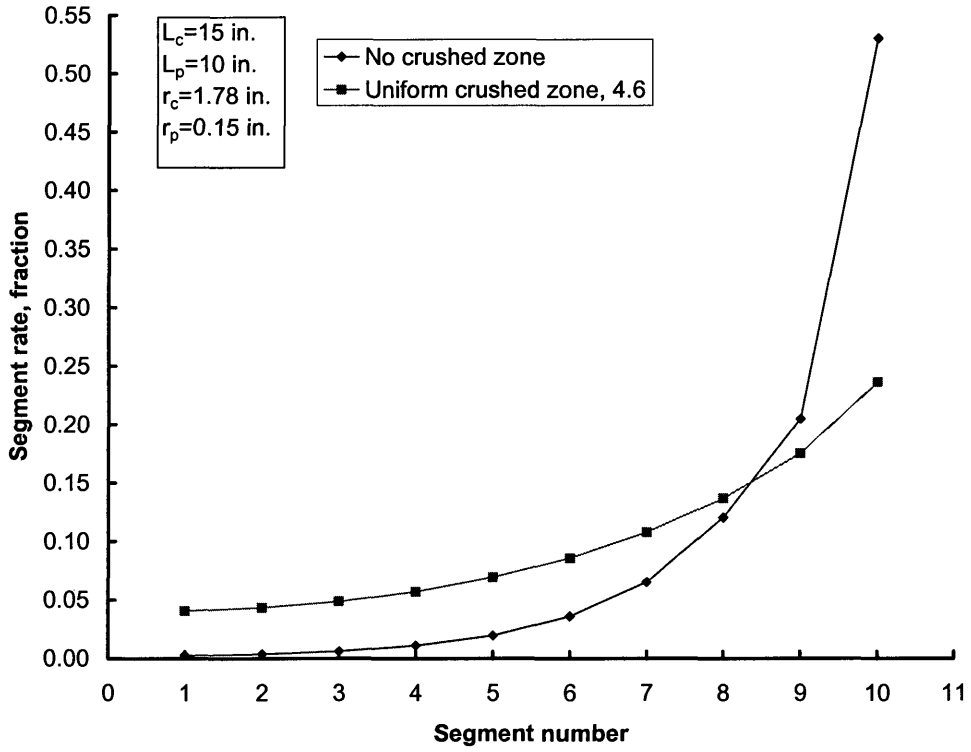

Figure 4.6 – Effect of skin factor on the flow distribution - Axial configuration.

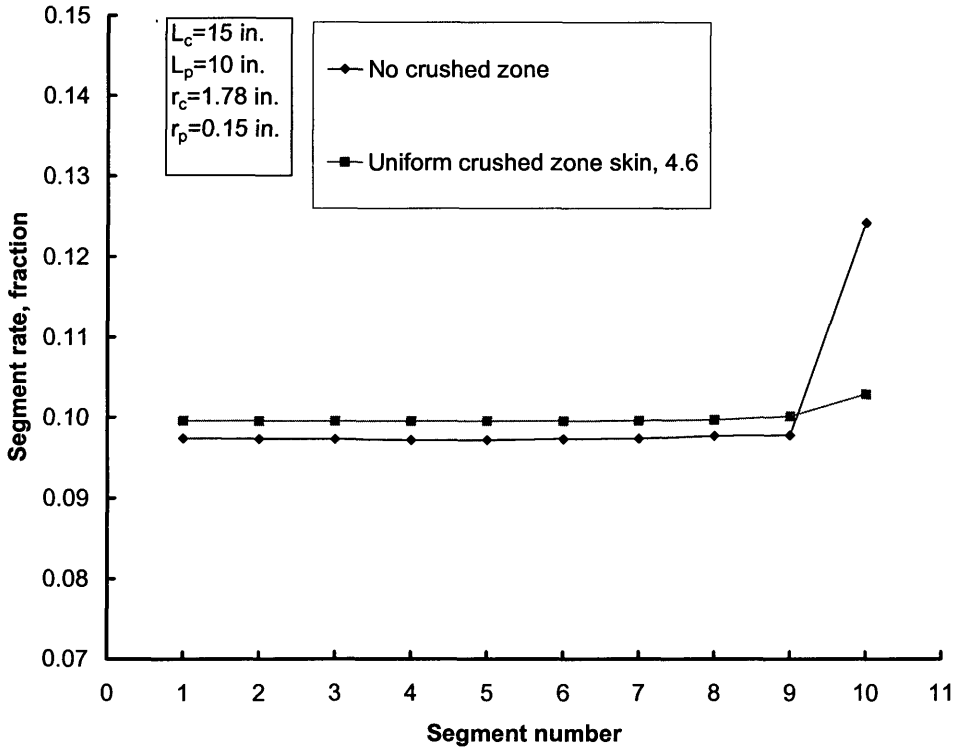

Figure 4.7 – Impact of perforation damage the on the flux distribution - Semi-radial case.

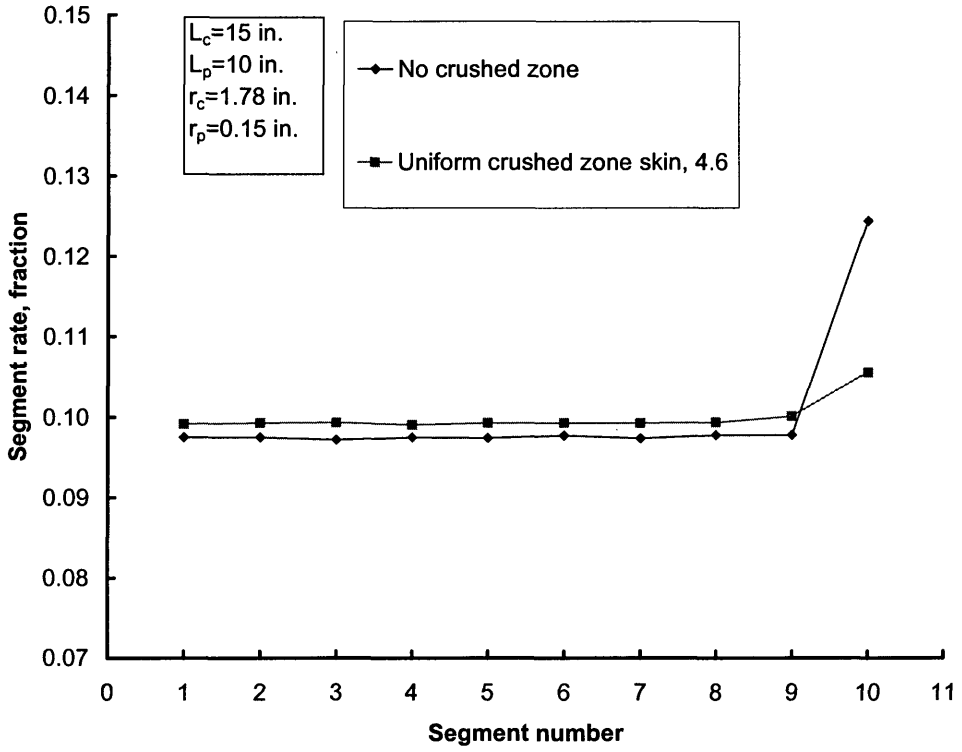

Figure 4.8 – Skin distribution effect on flux distribution – Radial-axial case.

In this section, we investigate the impact of non-uniform skin distribution on the post perforation flow performance. We consider three different skin distributions changing linearly along the perforation tunnel. Three cases are characterized by their end point skin values. In all three cases, the skin factor at the entrance is fixed at 5.5. In Case 1, the skin factor at the tip is 4.7. For Case 2, the skin factor at the tip is changed to 5. Finally, in Case 3, a skin factor of 5.3 is assigned to the tip of the perforation. In other words, Case 1 has stronger heterogeneity in its skin profile. Case 3 has the least non-uniform skin distribution. The results for all three non-uniform skin distribution cases are shown on Figs. 4.9, 4.10, and 4.11.

Fig. 4.9 displays the effect of different skin profile on the flux distribution along the perforation for an axial setup. The flux distribution is slightly influenced by three different skin profiles considered. It should be noted that although the first segment is assigned a skin value of 5.5 in all three cases, the contribution of the first segment is influenced by the complete skin profile along the perforation. It should be also observed that the stronger contrast in heterogeneous skin profile distorts the flux distribution further.

Fig. 4.10 shows the impact of three different skin profiles on the flux distribution in a core target with the semi-radial configuration. Compared to that in an axial core sample, the same skin profiles have stronger effect on the flux distribution in a semi-radial core target. However, similar to the axial core case, more heterogeneity in the skin profile promotes additional deviation in the flux distribution.

Fig. 4.11 illustrates the influence of the non-uniform skin distribution on the flow in a radial-axial core. A comparison of the data displayed in Figs. 4.10 and 4.11 demonstrates that, for all practical purposes, the results for the semi-radial and radial-axial core cases are nearly identical.

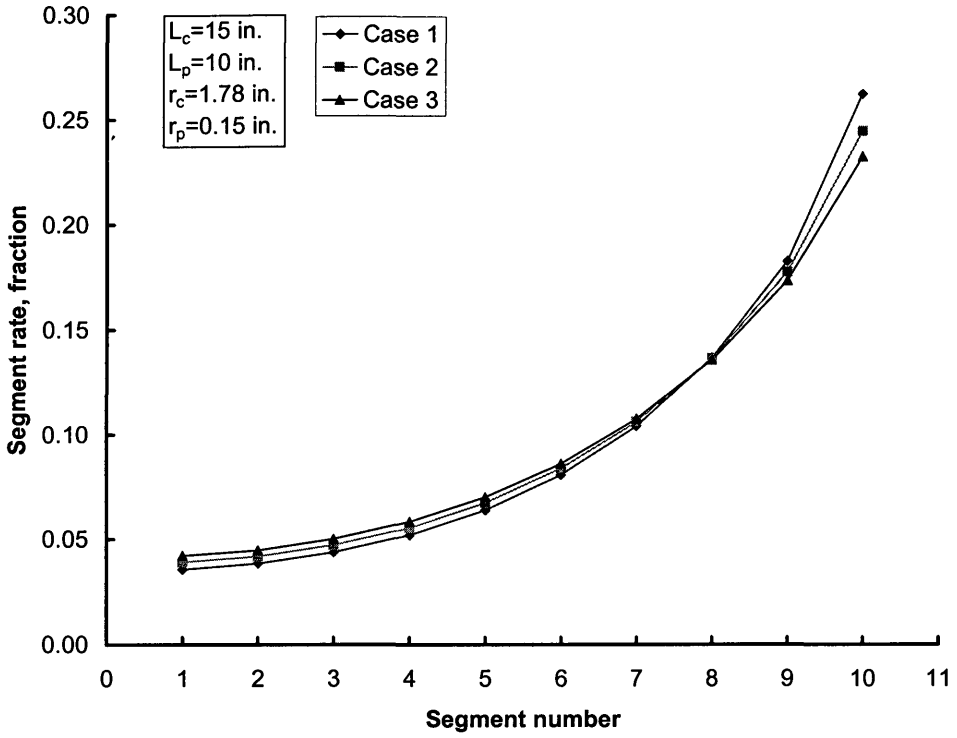

Figure 4.9 – Effect of non-uniform skin on flux distribution - Axial configuration.

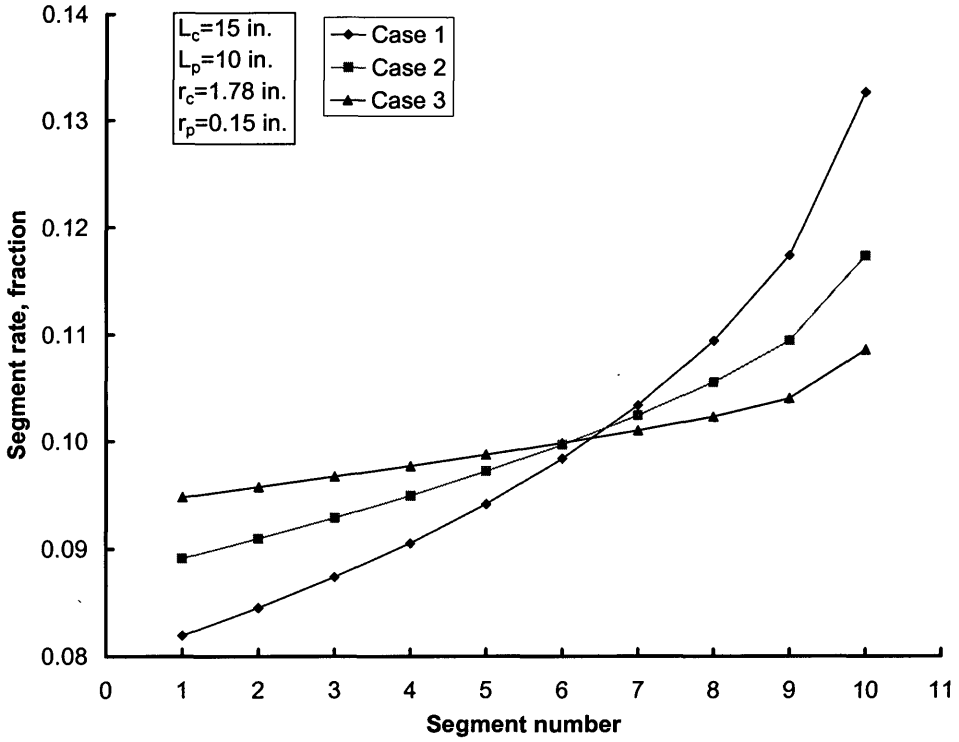

Figure 4.10 – Impact of non-uniform skin on flux distribution - Semi-radial case.

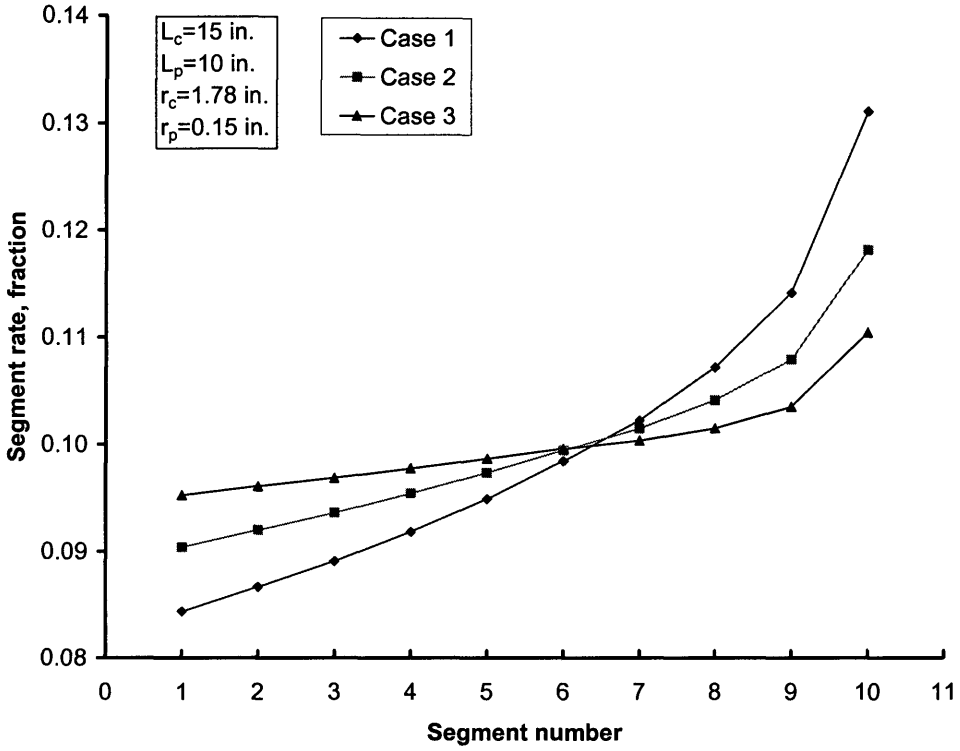

Figure 4.11 – Impact of non-uniform skin on flux distribution - Radial-axial case.

4.4 Effect of Test Configuration on Core Flow Efficiency

According to the API RP 19B, core flow efficiency is defined as the ratio of the measured flow rate influenced by the permeability impairment in the crushed zone to the ideal flow rate calculated from the flow models ignoring the effect of the permeability damage around the perforation tunnel. CFE is intended to quantify the permeability damage around the perforation tunnel. Unfortunately, besides the permeability impairment in the crushed zone, the CFE is also influenced by several other factors such as test configuration, core dimensions, and perforation dimensions. In this section, we investigate the influence of flow test geometry on core flow efficiency.

To understand the impact of flow test configuration on CFE, we use the basic data given in Table 4.1. Additionally, we consider a hypothetical jet perforator used in all three flow configurations. The jet perforator creates a crushed zone with r_{cz}=0.48 in. and k_{cz}=20 md yielding a skin factor of s_{cz}=5.6. Using the analytical flow models, we predict the flow rates under ideal and damaged perforation conditions for the axial, semi-radial, and radial-axial flow configurations. Once the ideal and measured flow rates are estimated, we calculate CFE values.

Fig. 4.12 shows the CFE as a function of test configuration and perforation length. It should be observed that CFE values for the semi-radial and radial-axial cases are nearly identical and independent of the perforation length. CFE values for semi-radial and radial-axial cases are around 0.3. On the other hand, CFE values for the axial case are somewhat influenced by the perforation length and are in the neighborhood of 0.8. Therefore, it is obvious that flow test configuration has a significant effect on CFE value.

A jet perforator with CFE value of 0.3 is not acceptable and should not be used in the field applications. On the other hand, a jet perforator with a CFE value of 0.8 may be acceptable for field use. If we use the hypothetical perforator on an axial core setup, it would be rated as a good/acceptable perforator. However, if the same hypothetical

perforator is tested on a semi-radial or radial-axial setup, its performance would be rates as poor.

The results presented above indicate that, given the same degree of permeability damage, the axial core setup shows significantly higher CFE values than the semi-radial and radial-axial flow configurations do. Hence, CFE value itself may not be a good indicator of the influence of the permeability damage around the perforation tunnel.

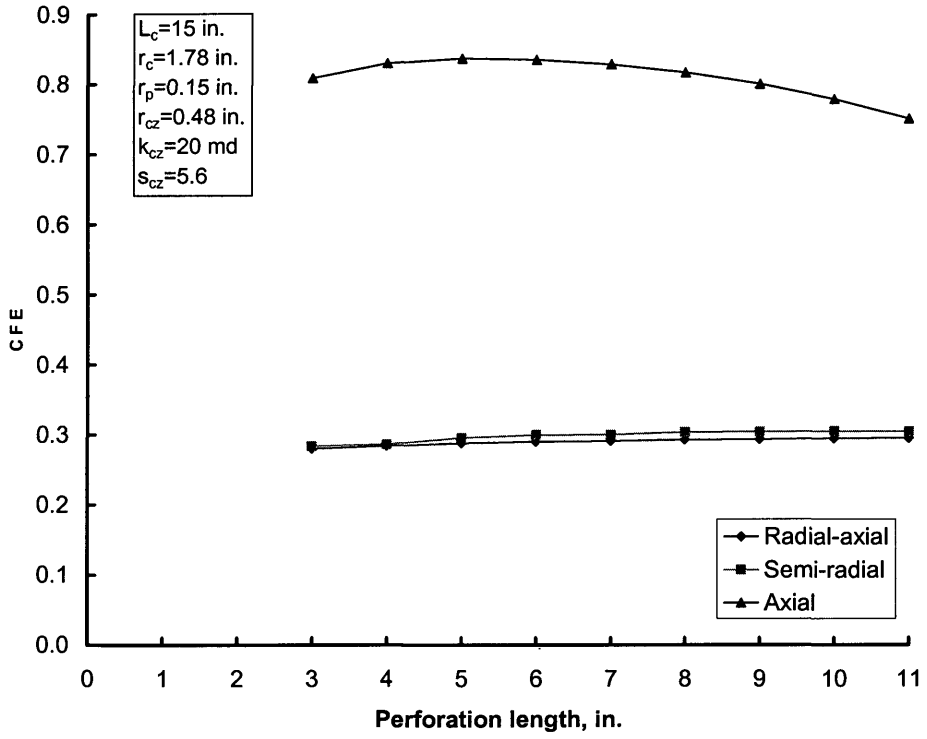

Figure 4.12- Impact of test configuration on CFE.

It may be worthwhile to investigate why the axial flow configuration yields high CFE values. For this purpose, we revisit the definition of CFE. CFE is defined as

$$CFE = \frac{q_{measured}}{q_{ideal}} \Big|_{\Delta p=\text{Constant}} \tag{4.1}$$

which assumes that the pressure drops across the undamaged and damaged perforations are the same and the flow rates are different. Alternatively, we may assume that the flow rates across the damaged and undamaged perforations are the same and the pressure drops are different. In such a case, CFE may be defined as

$$CFE = \frac{\Delta p_{ideal}}{\Delta p_{measured}} \Big|_{q=\text{Constant}} \tag{4.2}$$

where

$\Delta p_{measured}$ = Pressure drop in the damaged perforation case

Δp_{ideal} = Pressure drop in ideal undamaged case

The measured pressure drop in the damaged perforation is composed of two components.

$$\Delta p_{measured} = \Delta p_{ideal} + \Delta p_s \tag{4.3}$$

where

Δp_s = Additional pressure drop due to permeability damage in crushed zone

Combining Eqs. 4.2 and 4.3, we obtain

$$CFE = \frac{\Delta p_{ideal}}{\Delta p_{ideal} + \Delta p_s} = \frac{1}{1 + (\Delta p_s / \Delta p_{ideal})} \tag{4.4}$$

The additional pressure drop due to permeability damage is related to the skin factor and the permeability and the extent of the crushed zone as below.

$$\Delta p_s = \frac{q\,\mu}{2\pi\,\alpha\,L_p\,k_r} s_{cz} \tag{4.5}$$

$$s_{cz} = \left(\frac{k_r}{k_{cz}} - 1\right) \ln\left(\frac{r_{cz}}{r_p}\right) \tag{4.6}$$

Eqs. 4.5 and 4.6 indicate that as long as the permeability and extent of the crushed zone in all three flow configurations are the same, so would be the skin factors additional pressure drops due to damage in all three cases.

Examination of Eq. 4.4 reveals that, for a given constant Δp_s, the numerical value of CFE is controlled by the ideal pressure drop across the perforated core target, Δp_{ideal}.

As it has been demonstrated in previous sections, for a given constant pressure drop, the ideal flow rate on the axial core configuration is much lower than those on the semi-radial and radial-axial setups. On the other hand, if the comparison is made under constant flow rate conditions then it is obvious that the ideal pressure drop across the axial core setup would be much higher than those across the semi-radial and radial-axial configurations. Since $\Delta p_s = \text{Constant}$ in all three cases, the higher the ideal pressure

drop, the smaller the $\Delta p_s / \Delta p_{ideal}$ ratio. According to Eq. 4.4, a smaller $\Delta p_s / \Delta p_{ideal}$ ratio yields a higher CFE value.

Based on the argument presented above, it can be concluded that the same degree of permeability damage around perforation tunnel may yield significantly different CFE values on the axial and the other two configurations. Hence, CFE value may not be a good measure of perforation damage. Additional simulations have shown that CFE values for the axial setup is not sensitive to skin factors. Therefore, it is recommended to run the post-perforation flow tests on the semi-radial or radial-axial core setups.

4.5 Impact of Variable Perforation Radius

In the many models for the perforated wells and perforated API core targets, the perforation is assumed to be a hollow cylinder. However, experimental observations on the perforated core targets have proven that perforation radius vary along the perforation tunnel. Typically, perforation radius decreases along the perforation trajectory. Hence, the effect of variable perforation radius on the CFE should be investigated.

In a related study, using a three-dimensional finite element simulator, Ansah *et al.*[23] recently investigated the impact of variable perforation radius along the perforation tunnel on the well productivity. They have concluded that changes in perforation radius along the perforation axis have a negligible impact on the well productivity. To understand the influence of variable perforation radius on the well performance, one also may use the Karakas-Tariq[21] model and examine the sensitivity of well productivity to constant but different perforation radius. It should be reminded that Karakas-Tariq model considers constant perforation radius. However, we can change the perforation radius and investigate how the well productivity is influenced by perforation size (radius). Although

it is not reported here, such a study has also shown that perforation radius has a minor impact on the productivity of perforated wells.

In this study, using the analytical flow models, we investigated the effect of variable radius on core flow efficiency. We considered four cases. In the first case, the perforation radius varies from 0.2 to 0.05 in. along the perforation length. In the second, third, and fourth cases, perforation radius is constant and equal to 0.2, 0.125, and 0.05 in., respectively. 0.125 is the arithmetic average of the maximum and minimum radii in the variable radius case. We assigned the same uniform skin factor profile along the perforation in all four cases; s_{cz}=3.6. In all cases, the perforation is divided into twenty segments. CFE values are calculated for all three flow configurations. The results are reported in Table 4.2. As shown in Table 4.2, the CFE values for the variable radius and the third case, in which constant perforation radius is equal to arithmetic average of the variable case, are nearly equivalent. Therefore, it can be concluded that, similar to its' negligible impact on the well productivity, the variable perforation radius has a minor effect on the CFE.

Table 4.2 - The effect of variable perforation radius on CFE

	CFE		
Radius, in.	Axial	Semi-radial	Radial-axial
0.2-0.05	0.85	0.4	0.4
0.2	0.84	0.37	0.37
0.125	0.85	0.42	0.42
0.05	0.87	0.49	0.49

4.6 Effect of Core Size on CFE

As already stated in previous sections, CFE is intended to measure the degree of perforation damage created by the jet perforator. Unfortunately, several other factors such as the size of core target also affect CFE. In this section, we demonstrate that numerical value of CFE is influenced by the length and diameter of the core selected.

The API Recommended Practice 19B suggests minimum core diameters depending on the size of the explosive used. The API specifies that the target core should have a diameter larger than 4 in. when the explosive charge is less than 15 g. A core target with a diameter larger than 7 in. should be used if explosive charge weights more than 15 g.

To investigate the effect of core size, the basic input data reported in Table 1 and $r_p = 0.1$ in. are considered. The crushed zone permeability is 20 md and 4.6 is the value which yields a crushed zone skin of 4.6. First, keeping the perforation damage constant, we investigated the impact of core diameter on the CFE value. We calculated the CFE value on the axial and radial-axial configurations as a function of core diameter. Core diameter ranged from 2 in. to 7 in. The results are reported in Table 4.3.

Table 4.3 indicates that, in the core targets with the axial flow configuration, core radius has a significant impact on CFE value; CFE decreases as the core radius is increased. The CFE values for 2 in. and 7 in. diameter cores are 0.7 and 0.48, respectively. Eq. 4.4 may be revisited to understand the dependency of CFE on the core radius. Given the same additional pressure drop due to perforation damage, when the core radius is increased, the cross-sectional area open to flow increases, hence, the ideal pressure drop decreases. A smaller Δp_{ideal} yields a larger $\Delta p_s / \Delta p_{ideal}$. According to Eq. 4.4, a larger $\Delta p_s / \Delta p_{ideal}$ ratio decreases CFE value.

Table 4.3 indicates that, the radial-axial CFE values increase with an increase in core radius. This is due to the fact that, in the radial-axial flow configuration, most of the

flow takes place in radial direction. When we increase the core diameter, fluid travels a longer distance inside the core to reach to perforation. A longer flow path results in a larger ideal pressure drop, a smaller $\Delta p_s / \Delta p_{ideal}$ ratio, and a lower CFE.

In the second set of simulations, we investigated the effect of core length on CFE values. The results are tabulated in Table 4.4. It should be observed that CFE values for the radial-axial case do not change with the increasing core length. However, the axial CFE values are dependent on the core length. When the core length is increased, CFE value also increases.

Based on the simulated results shown in Tables 4.3 and 4.4, it could be stated that axial CFE values are markedly influenced by the size of the core target; hence, post-perforation flow tests should not be conducted on the axial configuration. The radial-axial CFE values do not seem to be affected by the core length; however, they are influenced by the core diameter. To have a stabilized radial-axial CFE value, core radius should be greater than 7 in.

Table 4.3 - Influence of core radius on CFE

	CFE	
r_c, in	Axial	Radial-axial
2	0.70	0.32
3	0.66	0.34
4	0.61	0.36
5	0.56	0.37
6	0.50	0.38
7	0.48	0.38

Table 4.4 - Effect of core length on CFE

L_c, in	CFE	
	Axial	Radial-axial
12	0.69	0.34
14	0.77	0.34
16	0.82	0.34

4.7 What to Make of CFE?

Relative merits of jet perforators are measured according to the procedure described in the API RP 19B. The rating of the perforators is based on perforation length, average perforation diameter, perforation diameter profile, and CFE measured on the perforated core target. The perforator performance data collected on the core targets are used to predict the performance of actual perforated wells. To understand how the API test data may be related to perforated well performance, we offer the discussion below.

CFE quantifies the impact of permeability damage in the crushed zone. CFE is the ratio of the actual post-perforation flow rate measured on the core to the theoretical ideal flow rate calculated from the mathematical models considering post-perforation flow geometry. The measured flow rate is influenced by the formation damage due to perforating. The ideal flow rate is calculated without considering the effect of formation damage. However, the post-perforation flow geometry is considered in the calculation of ideal flow rate. Mathematical expression for CFE is given in Eq. 4.1.

$$CFE = \frac{q_{measured}}{q_{ideal}} \Big|_{\Delta p=\text{Constant}} \tag{4.1}$$

The effect of perforating on a core target is not quite the same as that on a perforated well. The impact of perforating on the subsurface well is typically quantified in terms of well productivity ratio. Given a constant pressure drop, productivity ratio (PR) is defined as the ratio of measured flow rate in a perforated well to ideal flow rate in a vertical openhole. Measured flow rate carries the impact of perforations and the crushed zone around the perforation tunnels. Mathematically, PR is defined as below.

$$PR = \frac{q_{p-cz}}{q_{oh}} \Big|_{\Delta p=\text{Constant}} \tag{4.7}$$

where

q_{p-cz} = Flow rate in perforated well

q_{oh} = Flow rate in an ideal vertical openhole

Using the flow equations for openhole and perforated wells, it can be shown that PR can be expressed as

$$PR = \frac{q_{p-cz}}{q_{oh}} \Big|_{\Delta p=\text{Constant}} = \frac{\ln(r_e / r_w)}{\ln(r_e / r_w) + s_{pc}} \tag{4.8}$$

where s_{pc} is the perforation pseudoskin due to ideal perforation and the permeability impairment in the crushed zone around the perforation tunnel. Perforation pseudoskin may be computed using the procedure suggested by Karakas and Tariq.[21]

Notice that both CFE and PR definitions are similar. Both quantities are defined as the ratio of measured flow rates to ideal flow rates. As a result, one may ask the following question. If the same jet perforator is used to perforate a core target and subsurface well, would the PR of the perforated well be equal to or related to CFE of the

core? Before we answer the posed question, we should really scrutinize measured and ideal flow rates in both definitions. In both the CFE and PR definitions, the measured flow rate is influenced by the post-perforation flow geometry and permeability impairment in the crushed zone. However, the ideal flow rates in the CFE and PR definitions are somewhat different. The ideal flow rate in the CFE definition considers the post-perforation flow geometry but disregards the effect of the permeability damage around the perforation. On the other hand, the ideal flow rate in the PR definition is that for an openhole and ignores the impact of the post-perforation flow pattern and the permeability damage due to perforating. Therefore, CFE and PR cannot be the same. To make the definitions consistent, we also introduce a modified PR. The modified PR is the ratio of the measured flow rate in a perforated well with the crushed zone effect to the ideal flow rate in a perforated well without any permeability damage.

$$PR^* = \frac{q_{p-cz}}{q_p}\Big|_{\Delta p=\text{Constant}} \tag{4.9}$$

where

q_{p-cz} = Perforated well flow rate affected by perforations and crushed zone

q_p = Flow rate in an ideal perforated well without the crushed zone

Both q_{p-cz} and q_p are influenced by the post-perforation flow geometry. q_{p-cz} is additionally affected by the permeability damage around the perforation. However, q_p is not influenced by the permeability impairment in the crushed zone.

Using the flow equations, the modified PR can be expressed as

$$PR^* = \frac{\ln(r_e / r_w) + s_p}{\ln(r_e / r_w) + s_{pc}} \tag{4.10}$$

where s_p is the perforation pseudoskin due to ideal perforation only.

Although the modified PR definition is equivalent to CFE definition, this does not necessarily mean that a given jet perforator would give numerically the same/related CFE in the core target and modified PR in the perforated well.

In this section, we conduct a series of simulations to see if CFE could be related to PR or the modified PR. For the perforated core, the basic input data given in Table 4.1 is considered. For the perforated well, in addition to the data set reported in Table 4.5, phasing angle of zero, and shot density of 2 spf are used. It is assumed that the perforation length, perforation diameter, and the damage around the perforations are all the same in the perforated core and the well. The CFE for axial, semi-radial, and radial-axial configurations are computed using the flow models presented in Chapter 2. PR and the modified PR values for the perforated well are calculated using the Karakas and Tariq[21] algorithm. All the simulated results are presented in Table 4.6 and Table 4.7.

Table 4.5 - Input data for perforated well

h, ft	100
k_V, md	100
k_H, md	100
r_e, ft	850
r_w, in.	4.32
r_p, ft	0.24
L_p, in.	8.4
k_{cz}, md	20
r_{cz}, in.	0.72

Table 4.6 - CFE and PR comparison

k_{cz}	s_{cz}	CFE			Well Productivity Ratio	
		Axial	Semi-radial	Radial-axial	$PR=q_{p\text{-}cz}/q_{oh}$	$PR^*=q_{p\text{-}cz}/q_p$
5	14.9	0.60	0.08	0.08	0.31	0.39
10	7.1	0.73	0.16	0.16	0.46	0.58
20	3.1	0.82	0.30	0.30	0.60	0.75
30	1.8	0.88	0.43	0.42	0.67	0.84

In Table 4.6, although we consider the same perforation length, diameter, and damage in both the perforated core and well, the numerical values of CFE, PR and the modified PR differ substantially. The only general trend is that the higher the CFE in the core, the higher the well productivity.

Table 4.7 – Effect of shot density and phasing angle on well productivity ratio

Phasing angle	Shot per foot	$q_{p\text{-}cz}/q_{oh}$	$q_{p\text{-}cz}/q_p$
0	1	0.44	0.64
0	2	0.60	0.76
0	4	0.73	0.85
0	6	0.78	0.90
0	8	0.80	0.92
60	1	0.46	0.63
60	2	0.65	0.74
60	4	0.84	0.83
60	6	0.92	0.88
60	8	0.97	0.90
120	1	0.46	0.63
120	2	0.66	0.73
120	4	0.83	0.83
120	6	0.91	0.88
120	8	0.95	0.90

The results in Table 4.7 demonstrate that the perforated well productivity is substantially influenced by phasing angle and shot density which are not the parameters of concern in the case of the perforated core targets.

Based on the results presented in Tables 4.6 and 4.7, it can be stated that CFE measured on the perforated core may not be a good indicator for the productivity of the perforated well in subsurface conditions. There exists a general trend that a higher CFE on the core may translate to a higher well productivity. However, when it comes to actual numerical values, CFE and PR are not meaningfully related.

4.8 Criterion and Procedure to Rank Jet Perforators

All the results presented in this chapter indicate that the CFE value calculated for the perforated cores is not a good criterion to rank the relative merits of the jet perforators. The jet perforators should be rated based on their impact on the productivity of perforated wells. For this purpose, we suggest to transform CFE values from API flow tests to an equivalent skin factor that can be used in downhole conditions. The procedure is given below.

The average skin factor due to permeability impairment in the crushed zone is

$$s_{cz} = (k_r / k_{cz} - 1)\ln(r_{cz} / r_p) \tag{4.6}$$

Typically, we do not have information (direct measurement) about the degree of permeability damage and the extent of the crushed zone. However, we may be able to quantify the skin factor using the CFE value.

The additional pressure drop due to the skin factor around the perforation in a perforated core target is

$$\Delta p_s = \Delta p_m - \Delta p_{ideal} \tag{4.11}$$

On the other hand, assuming radial flow across the crushed zone, the additional pressure drop due to skin factor could be also expressed as

$$\Delta p_s = \frac{q_m \mu B_o}{2\pi \alpha k_r L_p} s_{cz-c} \tag{4.12}$$

where s_{cz-c} is the skin factor determined from the post-perforation flow tests conducted on the core targets and the same as s_{cz} given in Eq. 4.6. Combining Eqs. 4.11 and 4.12 and rearranging for the skin factor

$$s_{cz-c} = \frac{2\pi \alpha k_r L_p}{q_m \mu B_o}(\Delta p_m - \Delta p_{ideal}) \tag{4.13}$$

Manipulating the right-hand-side of Eq. 4.13,

$$s_{cz-c} = \frac{2\pi \alpha k_r L_p}{\mu B_o} \frac{\Delta p_m}{q_m}(1 - \frac{\Delta p_{ideal}}{\Delta p_m}) \tag{4.14}$$

Using the definition of core flow efficiency,

$$s_{cz-c} = \frac{2\pi \alpha k_r L_p}{\mu B_o} \frac{\Delta p_m}{q_m}(1 - CFE) \tag{4.15}$$

s_{cz-c} value belongs to a single perforation in the core target. However, we need to rescale this value for use in the wellbore models. The skin factor definition given in Eq.

4.6 also applies to the perforations around the wellbore in downhole conditions. However, Karakas and Tariq[21] have shown that, for downhole wellbore productivity computations, the skin factor needs to be rescaled as below.

$$s_{cz-wb} = \frac{\Delta z_p}{L_p} s_{cz-c} \tag{4.16}$$

Δz_p in Eq. 4.16 is the vertical distance between the adjacent perforations. Unfortunately, the scaling indicated in Eq. 4.16 would hold only in the absence of formation damage around the wellbore due to drilling and completion operations. If drilling and completion based formation damage exists around the wellbore, then we need to know not only the lumped parameter s_{cz-c} but also the permeability damage ratio of k_r / k_{cz}.

4.9 Evaluation of the Hsia and Behrmann Equivalent Skin Equation

Hsia and Behrmann[11] proposed a formulation to convert CFE to an equivalent crushed zone skin factor. Their equation is as follows

$$s_s = \left(\frac{1}{CFE} - 1\right) \ln\left(\frac{r_{cz}}{r_p}\right) \tag{4.17}$$

In the development of Eq. 4.17, Hsia and Behrmann[11] assumed that there is only a radial flow both inside the core and around the perforation. They neglected the flow inside the perforated core beyond the perforation tip. Here, we will investigate the accuracy of the equivalent skin equation proposed by Hsia and Behrmann.

To investigate the accuracy of the equivalent skin equation presented by Hsia and Behrmann, we considered the data set given in Table 4.1. For a given case, we assigned crushed zone skin values of $s_{cz} = 1$ and $s_{cz} = 10$ and simulated the flow in a radial-axial configuration for damaged and undamaged cases. Then, using the definition given in Eq. 4.1, we calculated CFE values. Finally, CFE values were used in Eq. 4.17 to convert the results to equivalent skin factor. We repeated the procedure for several perforation lengths and formation anisotropy. All the results are given in Tables 4.8, 4.9, and 4.10.

Table 4.8 reports the error analysis for the Hsia and Behrmann equivalent skin model for an isotropic core. When the perforation is long and the distance between the perforation tip and un-perforated end of the core is short, the Hsia and Behrmann equation works fine and

Table 4.8 – Error Analysis for the Hsia and Behrmann Equation, $k_r / k_x = 1$

	$s_{cz}=1$			$s_{cz}=10$		
L_p, in	CFE	s_s	% Error	CFE	s_s	% Error
3	0.68	1.11	11.00	0.18	11.01	10.1
5	0.69	1.07	7.00	0.19	10.57	5.7
12	0.7	1.03	3.00	0.2	10.21	2.1

Table 4.9- Error Analysis for the Hsia and Behrmann Equation, $k_r/k_x = 0.5$

	$s_{cz}=1$			$s_{cz}=10$		
L_p, in	CFE	s_s	% Error	CFE	s_s	% Error
3	0.64	1.17	17.3	0.15	11.48	14.8
5	0.66	1.09	9.9	0.17	10.88	8.8
12	0.69	1.04	3.8	0.18	10.32	3.2

Table 4.10- Error Analysis for the Hsia and Behrmann Equation, k_r/k_x=0.1

	s_{cz}=1			s_{cz}=10		
L_p, in	CFE	s_s	% Error	CFE	s_s	% Error
3	0.68	1.38	38	0.17	13.36	33.6
5	0.69	1.23	23	0.18	11.97	19.7
12	0.7	1.11	10.9	0.19	11.25	12.5

results in negligible errors. However, when the perforation is short, Hsia and Behrmann equation may inherit errors in the order of 10 %.

The effect of formation anisotropy on the error growth in the Hsia and Behrmann equation is summarized in Tables 4.9 and 4.10. Table 4.9 shows the error analysis for the Hsia and Behrmann equation in an anisotropic core with $k_r / k_z = 0.5$. The results indicate that the Hsia and Behrmann equation has more errors (up to 17%) in anisotropic formations. As can be seen in Table 4.10, when the formation anisotropy is increased, $k_r / k_z = 0.1$, the equivalent skin equation presented by Hsia and Behrmann may have errors up to 40 %.

Based on the results presented in Tables, 4.8 , 4.9, and 4.10, it may be stated that the equivalent skin equation proposed by Hsia and Behrmann may have considerable errors in highly anisotropic cores with short perforations.

CHAPTER 5

CONCLUSIONS

In this section, we summarize the results of the research study presented in this text. Some of the results pertain to the range of the data set considered in the study.

- Three analytical models to simulate the flow in the complicated post-perforation flow configurations are developed. The analytical models could mimic the flow in the perforated cores with the axial, semi-radial, and radial-axial setups. The analytical models consider arbitrary damage distribution and variable radius along the perforation axis.
- The analytical models are coded in a FORTRAN environment. The proposed solutions are compared against the models existing in the literature, and verified. The analytical solutions are general, available to public, and very fast and inexpensive to compute.
- The analytical models may be used to predict the flow rates in ideal undamaged perforations as well as damaged perforations. Therefore, using the models, post-perforation flow tests described in the API 19B may be analyzed, and core flow efficiency may be calculated.
- Using the analytical models, we investigated the impact of the axial, semi-radial, and radial-axial setups on the post-perforation flow tests. It is observed that the semi-radial and radial-axial setups yield nearly identical results. However, the results obtained on the axial test pattern differ substantially from those on the semi-radial and radial-axial configurations.

- For a given case, the axial configuration allows much lower flow rates across the core target compared to the semi-radial and radial-axial core setups.
- The flux distribution in the semi-radial and radial-axial core setups is almost uniform along the perforation. However, the flux exponentially increases along the perforation in an axial configuration.
- Permeability impairment in the crushed zone around the perforation tunnel may substantially change the flux distribution.
- Using the analytical models, a sensitivity study investigating the effect of the perforating parameters on the CFE has been conducted. It is demonstrated that the CFE is controlled by post-perforation flow geometry, core/perforation dimensions, permeability anisotropy, and the degree of formation damage.
- It is shown that the same degree of formation damage yields different CFE values in the axial and semi-radial/radial-axial post-perforation flow geometries. Given the same degree of permeability damage, the axial core setup shows significantly higher CFE values than the semi-radial and radial-axial flow configurations do. Hence, CFE value itself may not be a good indicator of the extent of the permeability damage around the perforation tunnel.
- The effect of variable the perforation radius is investigated. Up to a 10% difference may be observed in the CFE values for the variable perforation radius case and an equivalent uniform perforation radius case.
- The axial CFE values are markedly influenced by the size of the core target. Hence, post perforation flow tests should not be conducted on the axial configuration. The radial-axial CFE values do not seem to be affected by the core length; however, they are influenced by the core

diameter. To have a stabilized radial-axial CFE value, the core radius should be greater than 7 in.

- CFE measured on the perforated core may not be a good indicator for the productivity of the perforated well in subsurface conditions. There exists a general trend that a higher CFE on the core may translate to a higher well productivity. However, when it comes to the actual numerical values, CFE and productivity ratio of a perforated well are not meaningfully related.
- A method to convert the CFE data to an equivalent skin factor is presented. A procedure to rescale the skin factor from core targets to a perforated well is introduced.
- The accuracy of the equivalent skin equation presented by Hsia and Behrmann has been investigated. It is observed that the equivalent skin equation proposed by Hsia and Behrmann may have considerable errors in highly anisotropic cores with short perforations.

NOMENCLATURE

CFE = core flow efficiency

H = Heaviside unit step function

J_m = measured productivity index, STB/D/psi

J_{ideal} = ideal productivity index, STB/D/psi

k_h = horizontal permeability, md

k_v = vertical permeability, md

k_r = permeability in radial direction, md

k_x = permeability in axial direction, md

k_{cz} = permeability of crushed zone, md

$k_{//}$ = permeability in the direction parallel to bedding plane

$k_{\perp}$ = permeability in the direction perpendicular to bedding plane

L_p = perforation length, ft

L_c = length of the core, ft

n_s = shot density

p = pressure, psi

q = flow rate, STB/D

q_{ideal} = ideal perforation flow rate, STB/D

q_j = flow rate at the jth perforation, STB/D

q_m = measured perforation flow rate, STB/D

q_{oh} = openhole flow rate, STB/D

q_p = flow rate in an ideal perforated well without crushed zone, STB/D

$q_{p\text{-}cz}$ = flow rate of a perforated well with crushed zone skin, STB/D

r = radius, ft

r_c = core radius, ft

r_{czj} = radius of crushed zone around jth perforation segment, ft

r_e = reservoir radius, ft

r_{pj} = perforation radius at the jth segment, ft

r_w = wellbore radius, ft

s_{cz}= crushed zone skin

$s_{cz\text{-}c}$= crushed zone skin for perforated core

$s_{cz\text{-}wb}$= crushed zone skin for perforated well in downhole condition

s_p= pseudoskin due to ideal perforations without crushed zone

s_{pc}= pseudoskin due to perforations and crushed zone

s_s = equivalent skin factor defined by Hsia and Behrmann

Δp_s = additional pressure change because of skin, psi

Δp_{ideal} = pressure change in ideal case, psi

Δp_t = total pressure drop, psi

Δp_m = measured pressure drop, psi

Δp_j = pressure drop of the jth segment, psi

ΔL_{pj}= length of the jth segment, ft

Δz_p = spacing between perforations, ft

μ = viscosity, cp

θ = phasing angle

Subscripts:

c = core

czj = crushed zone of the jth perforation

i = ith perforation

j = jth perforation

m = measured

p = perforation

s = skin

r = radial direction

x = x-direction

t = total

REFERENCES

1. *Recommended Practices for Evaluation of Well Perforators*, API Recommended Practice 19B, First Edition (November 2000).
2. Bell, W.T., Breiger, E.F., and Harrigan, J.W.:"Laboratory Flow Characteristics of Gun Perforations," *JPT* (September 1972) 1095.
3. Klotz, J.A., and Krueger, R.S., and Pye, D.S.:"Effect of Perforation Damage on Well Productivity," *JPT* (November 1974) 1303.
4. Saucier, R.J., and Lands, J.F.:"A Laboratory Study of Perforations in Stressed Formation Rocks," *JPT* (September 1978) 265.
5. Regalbuto, J.A., and Riggs, R.S.:"Underbalanced Perforation Characteristics as Affected by Differential Pressure," *SPEPE* (February 1988) 83.
6. Behrman, L.A., and Halleck P.M.:"Efects of Wellbore Pressure on Perforator Penetration Depth," paper SPE 18243 presented at the 1988 SPE Annual Technical Conference and Exhibition, Houston, Texas, October 2-5.
7. Behrman, L.A., and Halleck P.M.:"Effect of Concrete and Berea Strengths on Perforator Performance and Resulting Impact on the New API RP-43," paper SPE 18242 presented at the 1988 SPE Annual Technical Conference and Exhibition, Houston, Texas, October 2-5.
8. Deo M., Tariq, S.M., and Halleck, P.M.: "Linear and Radial Flow Targets for Characterizing Down-hole Flow in Perforations," *SPEPE* (August 1989) 295.
9. Halleck, P.M., and Deo, M.:"Effects of Underbalance on Perforation Flow," *SPEPE* (May 1989) 113.

10. Behrmann et al.:"Measurement of Additional Skin Resulting from the Perforation Damage Zone," paper SPE 22809 presented at the 1991 SPE Annual Technical Conference and Exhibition, Dallas, Texas, October 6-9.
11. Hsia, T.Y., and Behrmann, L.A.:"Perforation Skin as a Function of Rock Permeability and Underbalance," paper SPE 22810 presented at 1991 SPE Annual Technical Conference and Exhibition, Dallas, Texas, October 6-9.
12. Pucknell, J.K., and Behrman, L.A.:" An Investigation of Damaged Zone Created by Perforating," paper SPE 22811 presented at 1991 Annual Technical Conference and Exhibition, Dallas, Texas, October 6-9.
13. Behie, A. and Settari, A.:"Perforation Design Models for Heterogeneous Multi-phase Flow," paper SPE 25901 presented at the 1993 Rocky Mountain Regional/Low Permeability Reservoirs Symposium, Denver, Colorado, April 12-14.
14. Rochon, J. et al.:" Viscous Fluid Characterize the Crushed Zone," *SPEDC* (September 1995) 198.
15. Dogulu, Y.S., *Modeling Laboratory Tests for Perforation Flow Performance*, Master of Science Thesis, Pennsylvania State University, State College, (December 1994).
16. Halleck, P.M. and Dogulu, Y.S.:"The Basis and Use of the API RP43 Flow Test for Shaped-Charged Oil Well Perforators," *Journal of Canadian Petroleum Technology* (May 1997) 53.
17. Devinder, S.A., and Sharma, M.M.:"The Nature of the Compacted Zone Around Perforation Tunnels," paper SPE 58720 presented at 2000 International Symposium on Formation Damage Control held in Lafayette, Louisiana, February 23-24.
18. Halleck, P.M., Grader, A.S. and Karacan, C.O.:" Mapping of Permeability Damage around Perforation Tunnel," *Journal of Energy Resources Technology* (September 2001) 205.
19. Folse, K. et al.:"Perforating System Selection for Optimum Well Inflow Performance," paper SPE 73762 presented at the 2002 SPE International Symposium and Exhibition on Formation Damage Control, Lafayette, Louisiana, February 20-21.

20. Tariq, S.M.:"Evaluation of Flow Characteristics of Perforations including Nonlinear Effects Using Finite Element Method," paper SPE 12781 presented at the 1984 SPE California Regional Meeting, Long Beach, California, April 11-13.
21. Karakas, M. and Tariq, S.:"Semi-Analytical Productivity Models for Perforated Completions," *SPEPE* (February 1991) 73.
22. Yildiz, T.:"Productivity of Selectively Perforated Vertical Wells," *SPEJ* (June 2002) 158.
23. Ansah, J., Proett, M.A., and Soliman, M.Y.:"Advances in Well Completion Design: A New 3D Finite-Element Wellbore Inflow Model for Optimizing Performance of Perforated Completions," paper SPE 73760 presented at the 2002 SPE International Symposium and Exhibition on Formation Damage Control in Lafayette, Louisiana, February 20-21.
24. Press, W.H et al., *Numerical Recipes,* Cambridge University Press, Cambridge, United Kingdom, 1998.
25. Vrbik, J.:"A Simple Approximation to the Pseudoskin Factor Resulting from Restricted-Entry," *SPEFE* (December 1991) 444.
26. Yildiz, T. and Cinar, Y.:"Inflow Performance and Transient Pressure Behavior of Selectively Completed Vertical Wells," *SPE Reservoir Eng.* (October 1998) 467.

APPENDIX A

A-1 Computer Code for Axial Flow Configuration

```
C     This program provides the total perforation flow rate and flow coming from each
C     segment of the perforation knowing the pressure drop along the perforation in API
C     Recommended Practice 19B for post-perforation, axial flow configuration.
C        q (stb/day)
C        dp (psi)
C        vi (cp)
C        kr, kz, kcz (md)
C        lc, lp (ft)
C        re, rp, rcz (ft)
         implicit double precision (a-h, o-z)
         dimension b(101,101),d(101)
C        reading information from the input file**************************
         write (*,*)'For crushed zone damaged case enter 1 and for undamaged
         * enter 0'
         read (*,*)y
         open (unit=5,file='api.xinp', status='unknown')
         read (5,*)dp
         read (5,*)vi
         read (5,*)xkr
         read (5,*)xkz
         read (5,*)xlc
```

```
      read (5,*)xlp
      read (5,*)rcz
      read (5,*)re
      read (5,*)rp
      read (5,*)nseg
      read (5,*)tol
      close (5)

      open (unit=8,file='api.xout', status='unknown')
      nsegp1=nseg+1
      write (8,*) 'nseg, nsegp1=', nseg, nsegp1
      xdlp=xlp/nseg
      pi=4.d0*datan (1.d0)
      coefm=8.d0*vi*xlc**2/1.127d-3/pi**4/rp/dsqrt (xkr*xkz)/xdlp**2
      xkcz=0.2*dsqrt (xkr*xkz)

C     setting the matrix coefficient*******************************
      b (1,1)=1.0d0
      b (1,2:nsegp1)=-1.d0
      b (2:nsegp1,1)=0.d0

      d (1)=0.0d0
      d (2:nsegp1)=dp

      do 1 j=2,nsegp1
         s=(dsqrt(xkr*xkz)/xkcz-1.)*dlog(rcz/rp)
        do 2 i=2,nsegp1
           sum1=-100.d0
```

```
      sum=0.d0
      do 3 n=1,10000
        xlam=(2*n-1)*pi*dsqrt(xkz/xkr)/(2.d0*xlc)
        xrp=xlam*rp
        xre=xlam*re
        xai=dsin((2*n-1)*pi*(i-1)*xdlp/(2.d0*xlc))
        xbi=dsin((2*n-1)*pi*(i-2)*xdlp/(2.d0*xlc))
        rnsi=xai-xbi
        xaj=dsin((2*n-1)*pi*(j-1)*xdlp/(2.d0*xlc))
        xbj=dsin((2*n-1)*pi*(j-2)*xdlp/(2.d0*xlc))
        rnsj=xaj-xbj
        xab=bessi0(xrp)/bessi1(xre)+bessk0(xrp)/bessk1(xre)
        xbb=-bessi1(xrp)/bessi1(xre)+bessk1(xrp)/bessk1(xre)
        xbess=xab/xbb
        term=xbess*rnsi*rnsj/(2*n-1)**3
        sum=sum+term

     if (mod(n,8).eq.0) then
              x=dabs(sum-sum1)/sum
              if (dabs(x).le.tol) then
                    go to 4
              end if
              sum1=sum
     end if
3       continue
4    if ((j.eq.i).and.(y==1)) then
       b (j,i)=coefm*sum+vi*s*141.2/(xdlp*xkr)
     else
```

```
                b (j,i)=coefm*sum
            end if
2           continue
1       continue
C       printing matrix coefficients*********************************
         do 5 L1=1,nsegp1
                write (8,50) L1,(b(L1,L2),L2=1,nsegp1)
50              format (3X,I3,11(2X,E11.4),3X,F6.3)
5       continue
         call matrix(nsegp1,b,d)

C        Printing flow rates*****************************************
        write (8,*)
        write (8,*)
        write (8,*)
        write (8,*) 'results'
        write (8,*)
        do 6 L3=1,nsegp1
            write (8,52) L3,d(L3)
52          format (3X,I3,3X,E11.4)
6       continue
        close (8)
C       stop
        end
```

A-2 Computer Code for Semi-Radial Flow Configuration

```
C       This program provides the total perforation flow rate and rate coming from each
Csegment of the perforation in API Recommended Practices 19B for post-perforation,
Cradial flow configuration

C       q (stb/day)
C       dp (ft)
C       vi (cp)
C       kr, kz, kcz (md)
C       Lc, Lp (ft)
C       re, rp, rcz (ft)

        implicit double precision (a-h, o-z)
        dimension  b (101,101), d (101)

C       reading data from output file**************************************
        write (*,*)'For crushed zone damaged case enter 1 and for undamaged
        * enter 0'
        read (*,*)y

        open (unit=5,file='apiradial.xinp',status='unknown')
        read (5,*)dp
        read (5,*)vi
        read (5,*)xkr
        read (5,*)xkz
        read (5,*)xlc
        read (5,*)xlp
```

```
      read (5,*)rcz
      read (5,*)re
      read (5,*)rp
      read (5,*)nseg
      read (5,*)tol
      close (5)

      open(unit=8,file='apiradial.xout', status='unknown')
      nsegp1=nseg+1
      write (8,*) 'nseg, nsegp1=', nseg, nsegp1
      xdlp=xlp/nseg
      pi=4.0d0*datan (1.0d0)
      coefm=-vi*xlc**2/1.127d-3/(pi**4)/rp/dsqrt(xkr*xkz)/xdlp**2
      xkcz=0.2*dsqrt(xkr*xkz)

C     setting the matrix coefficients*******************************
      b0=vi*dlog(re/rp)/(2.*pi*1.127d-3*xkr*xlc)
      b (1,1)=1.0d0
      b (1,2:nsegp1)=-1.0d0
      b (2:nsegp1,1)=b0

      d (1)=0.d0
      d (2:nsegp1)=dp

      do 1 j=2,nsegp1
         s=(dsqrt(xkr*xkz)/xkcz-1.)*dlog(rcz/rp)
         write (8,*)s
         do 2 i=2,nsegp1
```

```
 sum=0.0d0
sum1=-100.0d0
do 3 n=1,10000
      xlam=n*pi*dsqrt(xkz/xkr)/(xlc)
      xrp=xlam*rp
      xre=xlam*re
      xai=dsin(n*pi*(i-1)*xdlp/xlc)
      xbi=dsin(n*pi*(i-2)*xdlp/xlc)
      rnsi=xai-xbi
      xaj=dsin(n*pi*(j-1)*xdlp/xlc)
      xbj=dsin(n*pi*(j-2)*xdlp/xlc)
      rnsj=xaj-xbj
      xab=bessi0(xrp)/bessi0(xre)-bessk0(xrp)/bessk0(xre)
      xbb=bessi1(xrp)/bessi0(xre)+bessk1(xrp)/bessk0(xre)
      xbess=xab/xbb
      term=xbess*rnsi*rnsj/n**3
      sum=sum+term
      if (mod(n,8).eq.0) then
        x=(sum-sum1)
        if (dabs(x).le.tol) then
          go to 4
        end if
        sum1=sum
      end if
3     continue
4   if ((j.eq.i).and.(y==1)) then
  b (j,i)=coefm*sum+vi*s*141.2/(xdlp*xkr)
    else
```

```
                b (j,i)=coefm*sum
              end if
2           continue
1         continue

C     printing matrix coefficients*******************************
          do 5 L1=1,nsegp1
             write(8,50) L1,(b(L1,L2),L2=1,nsegp1)
50           format(3X,I3,11(2X,E11.4),3X,F6.3)
5         continue
      call matrix(nsegp1,b,d)

C     printing flow rates ***************************************
          write (8,*)
          write (8,*)
          write (8,*)
          write (8,*) 'results'
          write (8,*)
          do 6 L3=1,nsegp1
             write (8,52) L3,d(L3)
52           format (3X,I3,3X,E11.4)
6         continue
          close (8)
          stop
          end
```

A-3 Computer Code for Radial-Axial Flow Configuration

```
C     This program provides the perforation total flow rate and rates coming from each
Csegment along the perforation in API Recommended Practices 19B for post-perforation,
Caxial_radial flow configuration

C       q(stb/day)
C       dp(ft)
C       vi(cp)
C       kr, kz, kcz (md)
C       Lc, Lp (ft)
C       re, rp, rcz (ft)

        implicit double precision (a-h, o-z)
        dimension  b (101,101), d (101)

C       reading the information from the input file**********************
        write (*,*)'For crushed zone damaged case enter 1 and for undamaged
        * enter 0'
        read (*,*)y

        open (unit=5,file='apiradial_axial.xinp', status='unknown')
        read (5,*)dp
        read (5,*)vi
        read (5,*)xkr
        read (5,*)xkz
        read (5,*)xlc
        read (5,*)xlp
```

```
      read (5,*)rcz
      read (5,*)re
      read (5,*)rp
      read (5,*)nseg
      read (5,*)tol
      close (5)

      open (unit=8,file='apiradial_axial.xout', status='unknown')
      nsegp1=nseg+1
      write (8,*) 'nseg, nsegp1=', nseg, nsegp1
      xdlp=xlp/nseg
      pi=4.0d0*datan(1.0d0)
      coefm=-vi*16.*xlc**2/1.127d-3/(2.*pi**4)/rp/dsqrt(xkr*xkz)/xdlp**2
      xkcz=0.2*dsqrt(xkr*xkz)

C     setting the matrix coefficients**************************
      b (1,1)=1.0d0
      b (1,2:nsegp1)=-1.0d0
      b (2:nsegp1,1)=0.0d0

      d(1)=0.d0
      d(2:nsegp1)=dp
      do 1 j=2,nsegp1
            s=(dsqrt(xkr*xkz)/xkcz-1.)*dlog(rcz/rp)
            do 2 i=2,nsegp1
                  sum=0.0d0
                  sum1=-100.0d0
                  do 3 n=1,10000
```

```
                xlam=(2*n-1)*pi*dsqrt(xkz/xkr)/(2.*xlc)
                xrp=xlam*rp
                xre=xlam*re
                xai=dsin((2*n-1)*pi*(i-1)*xdlp/(2.*xlc))
                xbi=dsin((2*n-1)*pi*(i-2)*xdlp/(2.*xlc))
                rnsi=xai-xbi
                xaj=dsin((2*n-1)*pi*(j-1)*xdlp/(2.*xlc))
                xbj=dsin((2*n-1)*pi*(j-2)*xdlp/(2.*xlc))
                rnsj=xaj-xbj
                xab=bessi0(xrp)/bessi0(xre)-bessk0(xrp)/bessk0(xre)
                xbb=bessi1(xrp)/bessi0(xre)+bessk1(xrp)/bessk0(xre)
                xbess=xab/xbb
                term=xbess*rnsi*rnsj/(2*n-1)**3
                sum=sum+term
                if (mod(n,8).eq.0) then
                   x=(sum-sum1)
                   if (dabs(x).le.tol) then
                      go to 4
                   end if
                   sum1=sum
                end if
3               continue
4               if ((j.eq.i).and.(y==1)) then
                   b(j,i)=coefm*sum+vi*s*141.2/(xdlp*xkr)
                else
                   b(j,i)=coefm*sum
                end if
2           continue
```

```
1       continue

C       printing the matrix coefficients**********************************
        do 5 L1=1,nsegp1
           write (8,50)L1,(b(L1,L2),L2=1,nsegp1)
50         format (3X,I3,11(2X,E11.4),3X,F6.3)
5       continue
        call matrix(nsegp1,b,d)
C       printing the total flow rate and flow rate from each segment**********
        write (8,*)
        write (8,*)
        write (8,*)
        write (8,*) 'results'
        write (8,*)
        do 6 L3=1,nsegp1
           write (8,52) L3,d(L3)
52         format (3X,I3,3X,E11.4)
6       continue
        close (8)
        stop
        end
```